Texas A&M University

Mechanical Engineering Department

Turbomachinery Laboratory

BUMP-TYPE FOIL BEARING STRUCTURAL STIFFNESS: EXPERIMENTS AND PREDICTIONS

Research Progress Report to the Turbomachinery Research Consortium

by

Dario Rubio

Research Assistant

Luis San Andrés

Professor

TRC-B&C-5-03

May 2003

TRC Project:

Identification of Structural Stiffness and Damping in Foil Bearings

BUMP-TYPE FOIL BEARING STRUCTURAL STIFFNESS: EXPERIMENTS AND PREDICTIONS

Executive Summary

Foil gas bearings (FB) satisfy many of the requirements noted for novel oil-free turbomachinery. However, FB design remains largely empirical, in spite of successful commercial applications. Four bump-type foil bearings were acquired in 2002. The bearings, 1.50 in length and diameter, contain a single foil (0.004 in), Teflon coated, supported on 25 bumps, height and pitch equal to 0.015 in and 0.18 in, respectively. The nominal radial clearance is 1.4 mils for a 1.5 in journal. A simple test set up was assembled to measure the FB deflections resulting from static loads. The tests were conducted with three shafts, one of 1.5 in diameter; and the other two with +1 mil and –1 mil larger (smaller) diameters. The larger diameter shaft induces a degree of preload into the FB structure.

Static measurements show nonlinear FB deflections and varying with the orientation of the load relative to the foil spot weld. Loading and unloading tests evidence a hysteresis effect. The FB structural stiffness increases as the bumps-foil radial deflection increases (hardening effect). The estimated structural stiffnesses obtained from two bearings, identical in construction, also differ. The assembly preload results in notable stiffness changes, in particular for small radial loads.

A simple physical model assembles individual bump stiffnesses and renders predictions for the FB structural stiffness as a function of the bump geometry and material, dry-friction coefficient, load orientation, clearance and preload. The model predicts well the test data, including the hardening effect. The uncertainty in actual clearance (gap) upon assembly of a shaft into a FB affects most the predictions.

TABLE OF CONTENTS

LIST OF TABLES

LIST OF FIGURES

NOMENCLATURE

C_{nom}	Nominal Clearance [mil]
D	Load capacity coefficient for CFB
D_i	Shaft Diameter [in]
E	Young modulus [psi]
F	Static Load [lb]
F_X	Reaction force in the X direction [lb]
F_ξ	Reaction force in the radial direction [lb]
F_Y	Reaction force in the Y direction [lb]
H_i	Actual bump height [mil]
h	Bump Height [in]
k	Structural foil bearing stiffness [lb/mil]
K_a	Average structural stiffness [lb/mil]
K_F	Free bump structural stiffness [lb/mil]
K_i	Structural stiffness [lb/mil]
K_I	Intermediate bump structural stiffness [lb/mil]
K_W	Welded bump structural stiffness [lb/mil]
l_o	Half of bump length [in]
N	Number of data set points
p	Bump pitch [in]
p_xL	Projected area of top foil [in^2]
r	Bearing preload [mil]
SEE	Standard error of an estimate [lb/mil]
s_f	Compliance for the free bump [mil]
s_w	Compliance for the welded bump [mil]
t	Bump foil thickness [in]
U_F	Uncertainty of the dynamometer [lb]
U_k	Bearing stiffness uncertainty [lb/mil]
U_V	Uncertainty of the multimeter [V]
U_x	Uncertainty of the dial gauge [mil]
x	Deflection [mil]
X	Shaft displacement in the X direction [mil]
Y	Shaft displacement in the Y direction [mil]
α	Bump height angle [deg]
β	Angular position to evaluate structural stiffness [degree]
δ	Bump deformation [mil]
η	Transverse deflection of bumps [mil]
μ	Friction coefficient
θ	Foil bearing angular position angle [degree]
υ	Poisson's ratio
ζ	Normal deflection of bumps [mil]

I. INTRODUCTION

Gas foil bearing technology has made significant progress during the last 30 years. Compliant foil bearings (CFB) fulfill most of the requirements of novel oil-free turbomachinery by increasing tenfold their reliability in comparison to rolling elements bearings, for example [1]. Foil bearings are made of one or more compliant surfaces of corrugated sheet metal and one or more layers of top foil surfaces. The compliant surface provides bearing stiffness and comes in several configurations such as bump-type (Figure 1), leaf-type (Figure 2) and tape-type, among others.

In bump-type foil bearings, the top foil is supported by compliant bumps and elastically deforms under pressure created by a hydrodynamic film. The bearing stiffness combines that resulting from the deflection of the bumps and also by the hydrodynamic film generated when the shaft rotates. Damping arises due to the relative motion between the bumps and the top foil or between the bumps and the bearing wall, i.e. Coulomb type damping [2].

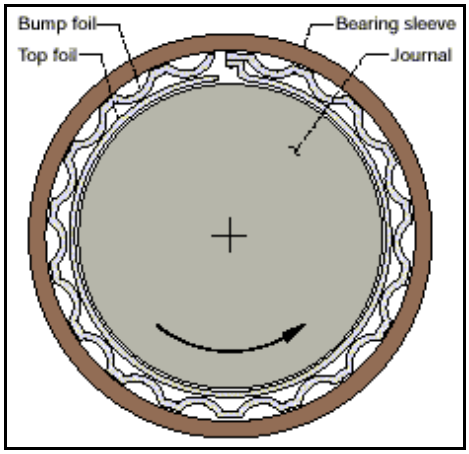

Figure 1 Bump-Type Gas Foil Bearing (Source: NASA Web Site)

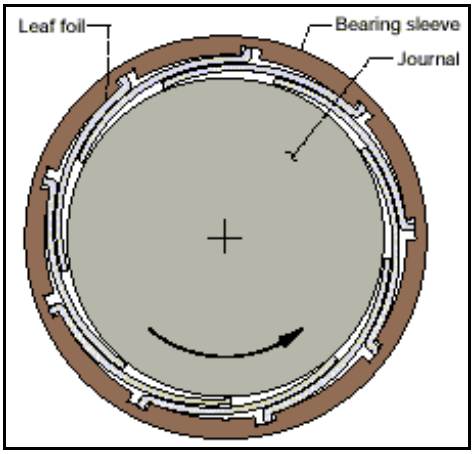

Figure 2 Leaf-Type Gas Foil Bearing (Source: NASA Web Site)

CFBs offer significant advantages over rolling elements bearings such as requiring fewer parts to support the rotating assembly without the need of oil lubrication supply [3]. These features lead to a more reliable performance of the rotor bearing system. Foil bearings also have a significant impact on the performance of turbomachines, For instance, the foil bearing hydrodynamic action allows for a large load capacity and high speed operation [1]. In terms of rotor stability, foil bearings allow larger shaft misalignments than plain journal bearings because of the ability of the top foils and bump foils to comply and deflect under misalignment. Misalignments of the shaft due to tolerance build-ups, centrifugal shaft growth, and differential thermal expansion are absorbed by the expansion of the top foil.

CFBs generally operate with ambient air. However, some specific applications use other lubricants such as helium, xenon, liquid nitrogen and liquid oxygen among others [3]. Remarkable improvements in high temperature limits are obtained by using coatings (solid

lubricants). Process gases can operate at very high temperatures without chemically breaking down as opposed to conventional lubricant oils. In addition, oil lubricants lead to larger power losses due to friction at the interface between the fluid and bearing shell.

Currently, applications of foil bearings can be found in several types of rotating machine equipment. The most common application is on Air Cycle Machines (ACM), the heart of the Environment Control System in aircrafts. In fact, the first foil bearing developed by Garrett AiResearch in the mid 1960's was designed to operate in an ACM. The foil bearing proved to be far more reliable than rolling element bearings. Nowadays, almost all Air Cycle Machines in military and civil aircraft, as well as many ground vehicles, utilize foil bearings. Other applications of foil bearings include oil-free cryogenic turboexpanders for gas separation plants, auxiliary power units for various aerospace and ground vehicles, automotive gas turbine engines, vapor-cycles centrifugal compressors, and commercial air/gas compressors [3].

Despite the level of progress reached during recent years in foil bearing technology, there are still considerations to take into account to model and to predict accurately the static and dynamic forced performance of foil gas bearings. The present research provides reliable measurements of the static structural stiffness of bump-type foil bearings. The results serve as benchmark for calibration of analytical tools under development at TAMU.

II. LITERATURE REVIEW

Literature concerned with static and dynamic characteristics of foil bearings is quite extensive. The results achieved in previous works represent important background for the current research project. Some of the technical papers related to the topic of this paper are detailed below as well as the relevant results obtained in each of the studies.

Agrawal [1] summarizes the chronological progress of foil air bearings for turbomachinery during the last 25 years. Descriptions of various machines that are in production are provided. For example, the foil bearing air cycle machine on the 747 aircraft has demonstrated a mean time between failures (MTBF) in excess of 100,000 hours. Also, many advantages of foil air bearings are noted and various designs of foil air bearings currently in use, with their relative merits, are described. Analytical methods, their limitations, and their relationship with test results are noted. In addition, descriptions of various machines, other than air machines, built and tested with gas process fluids are described. Various high speed turbomachines, including high temperature applications, can be designed and developed using air foil bearings, increasing efficiency and reducing the cost of these machines.

Ku and Heshmat [2] develop a method to obtain the stiffness of a complaint foil bearing. The results show the dependency between the bump foil stiffness and several parameters such as the bump configuration, surface coating and the presence or absence of lubrication. A change in the bump thickness only has small effect on the local stiffness, but reducing the pitch of the bump increases the local stiffness. In regard to coatings, high friction coefficients result in high values of bump stiffness. The presence or absence of lubrication does not make a remarkable difference in the bump stiffness. From the test results obtained, the bump pitch is the most important design

parameter in air foil bearings. In the same sense, Ku [4] describes the effects of bearing parameters, such as static loads, dynamics displacement amplitudes, bumps configurations, pivot locations and surface coating in the dynamic characteristics of foil bearings. Experimental and analytical results show that as the load increases or dynamic displacement amplitude decreases, the dynamic structural stiffness increases.

Iordanoff [5] proposes a rapid method design for the elastoaerodynamic problem in foil thrust bearings based on the solution of Reynolds equations. Bearing performance is identified three different approaches. These methods are applied successfully for the design of a 80 mm O.D., 40 mm I.D. thrust bearing with significant improvements in load capacity. Experimental results of thrust foil bearing parameters agree well with the complete direct calculations. Iordanoff also develop formulae for prediction of a single bump foil stiffness with a free end and welded end constrains.

Della Corte and Valco [6] introduce a simple "rule of thumb" method to estimate the load capacity in foil air journal bearing. The method relates the bearing load capacity to the bearing size and the speed through an empirically based load capacity coefficient, D. Based on previous experiments, DellaCorte and Valco determine that the load capacity is a linear function of the surface velocity and bearing projected area and the load capacity coefficient, D, is related to the design features of the bearing and operations conditions. Thee generations of foil bearings are selected to validate this method. First generation foil bearing developed in the 70's reaches load capacity coefficient of $D = 0.4$. However, latest foil bearing designs improve load capacity with a D coefficient up to 1.4. Larger D coefficients values are attained by adjusting geometry details in the foil support structures and the ability to adapt these details to a specific application.

Chen et al. [7] present an applications example of the successful replacement of a tape-type foil bearing for a bump-type foil bearing in a helium turbocompressor. Both bearing types are described, as are the steps involved in the design and fabrication of the bump bearing, and results of a comparison test between the original and replacement bearings. Methods to analyze bump-type foil bearing with commercially available software are reviewed to further emphasize the inherent simplicity of this bearing. Frictional torque of foil bearings is greater when the rotor starts up and decreases when the rotor speed is high enough to generate a hydrodynamic film. The same characteristic is observed from the coast down response of the rotor. Steady state and transient tests are also performed. The tests show that the implementation of the bump-type foil bearing increased the critical speed of the original system because the bearing stiffness is likely to be greater than that of the previous design (tape-type foil bearings).

Howard and Della Corte [8] discuss the influence of temperature, load, and speed in foil bearing stiffness and damping coefficients. A two degree of freedom system models the stiffness and damping due to friction and viscous contact between the surfaces. According to the results obtained, stiffness can be expected to change by a factor of two or three with large changes in load or speed. Another important result achieved from this study explains that the damping mechanism in foil bearings can be explained by frictional and viscous sources. Both sources are controlled by selecting an appropriate material for coating the surfaces in contact and also by changing parameters such as load or speed thus yielding changes in frictional damping, i.e., if more damping is needed, increasing frictional coefficients alone will not be sufficient. The

bearing must also be able to activate the frictional damping mechanism in order to reap the benefits from increased friction. The frictional damping can be activated by heavily loading the bearing so that the foil deflection can be encouraged and frictional damping, already present in the system, be more beneficial.

III. FOIL BEARING DESCRIPTION

Two bump-type foil bearings[1], as shown in Figures 1 and 2, are tested to provide reliable information on the foil bearing structural parameters. The foil bearing manufacturer numbers are 047 and 043; and hereby referred as CFB1 and CFB2, respectively. The main components of the test foil bearings are:

a) *Bearing Sleeve:* A rigid cylindrical ring supporting the bump foils and the top foil.

b) *Top foil:* The top foil is a thin flat metal sheet attached to the bearing sleeve at one end and free at the other end.

c) *Bump foil:* The bump foil configuration consists of four strips, each with five bumps, aligned axially. The end of a strip is welded to the bearing sleeve while the other end is free, as shown in Figure 4. A total of five segments are placed around the bearing sleeve. Note that each segment is welded at one end and free at the other. The test foil bearings have a total of twenty five bumps around the bearing sleeve.

d) *Spot Weld:* Weld line attaching the top foil and the bump foil strips to the bearing sleeve. The spot weld location is characterized by the absence of bumps and it spans approximately 10°. The spot weld constrains the movement of the top foil and the bump foil at one end (fixed end).

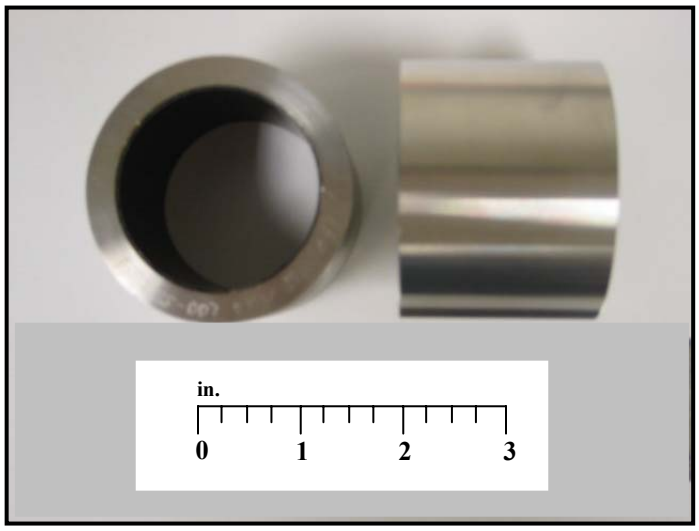

Figure 3 Test Foil Bearings

[1] Four foil bearings were acquired from Foster-Miller Technologies, January 2002.

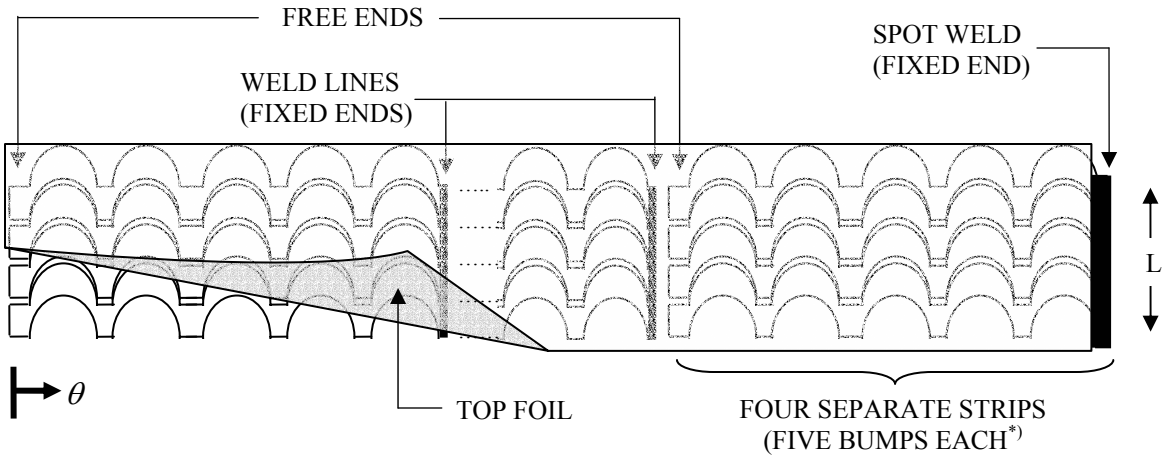

* There are five segments of four strips along the angular coordinate *(θ)*

Figure 4 Schematic View of Extended Bump Strips

Notice that Figure 4 defines an angular coordinate system (θ) at the foil free end. The foil spans 350°, since the spot weld extents approximately 10°.

This foil bearing design constrains the direction of shaft rotation to only one direction. Due to the hydrodynamic film created by rotor spinning, the top foil expands resulting in a larger film thickness than in conventional rigid wall bearings. At start up, the back of the foil is in contact with the bump foils and the outer side of the foil is in contact with the journal. As the rotor spins to a sufficiently high speed (i.e. when lift off occurs), the top foil expands as air is dragged into a thin annular film between the foil and the shaft. The compliant inner surfaces of the foil bearing allow larger shaft misalignment than conventional rigid wall journal bearings.

III.1 FOIL BEARING PARAMETERS AND DIMENSIONS

Table 1 shows the foil bearing parameters and nominal dimensions. Measurements of the nominal dimensions are performed on CBF1 and CFB2. Since the foil bearing inner surface is flexible, the measurement of the inner diameter is obtained for several radial and axial positions. Table 1 shows, among other parameters, the inner diameter average of all these measurements. Nominal dimensions and parameters from the CFB manufacturer are also shown in Table 1. According to the foil bearing manufacturer, the top foil is coated with spray-on coating Emralon 33, applied to a thickness of 0.001 inch. Ku et al. [2, 9] explains that the most important design parameter in foil bearing is the bump pitch. By reducing the pitch of the bump, the local stiffness increases dramatically. As regards to coating, the higher it dry friction coefficient the higher the CFB stiffness. Increases in bump thickness or height and decreases in bump length produces higher stiffnesses.

Table 1 Nominal Dimension and Test Foil Bearing Parameters [2]

Parameters	CFB 1	CFB 2	CFB Manufacturer Data
Outer Diameter (in.) [3]	2.0096	2.0086	N/A
Foil Thickness (in.) [3]	0.0062	0.0062	0.004
Number of Bumps	25	25	25
Bump Pitch (in.) (deg)	0.1825 (13)	0.1822 (13)	0.18
Bump Length (in.)	0.16	0.16	N/A
Axial Length (in.) [3]	1.5096	1.5052	N/A
Bump Foil Thickness (in.)	N/A	N/A	0.004
Bump height (in.)	N/A	N/A	0.015
Poisson's Ratio	N/A	N/A	0.29
Modulus of Elasticity (Psi)	N/A	N/A	31,000,000
Inner Diameter Ave. (in.) [4]	1.5100	1.5082	1.5028
Weight (lb)	0.613	0.613	N/A
Nominal Clearance [in] [5]	N/A	N/A	0.0014

IV. MEASUREMENTS TO DETERMINE CFB STIFFNESS

Static tests are performed on CFB1 and CFB2 to obtain the foil bearing structural characteristics. These tests aim to identify structural stiffness as a function of the bearing deflection and applied load. The hysteretic phenomenon on the CFBs is also addressed.

IV.1 EXPERIMENTAL PROCEDURE

A simple test setup is assembled on a lathe. Figures 5 and 6 depict the main components of the test setup, consisting of the test foil bearing, a copper shaft, a dynamometer, and two displacement instruments, i.e. dial gauge and eddy current sensor. The two test foil bearings are shown in Figure 3, and Table 1 shows the bearings nominal dimensions and parameters. The dynamometer is clamped to the lathe tool holder and moves horizontally by rotating the tool holder positioning mechanism. The CBFs are tested with three different shafts of diameters, 1.5000 in. (D_1), 1.5001 in. (D_2), and 1.499 in. (D_3). Therefore; different assembly bearing preloads are achieved. Shaft diameters are referred in this report as D_1, D_2, and D_3, respectively, as mentioned above.

[2] Appendix A shows the bearing nominal parameters in SI units
[3] Measurements taken with a micrometer gauge. Uncertainty: ± 0.0005 in.
[4] Measurements taken with a telescope gauge and a micrometer vernier. Uncertainty ± 0.0005 in.
[5] Nominal Clearance for a shaft diameter of 1.500 in

Figure 5 Test Setup for Static Experiments. Side View

Static measurements using a D_1 = 1.500 in. nominal shaft diameter are performed with a dial gauge and an eddy current sensor. While static measurements using D_2 = 1.501 in., and D_3 = 1.499 in. shaft diameters are performed with an eddy current sensor. The two displacement sensors are held in position by a giraffe neck holder located 180 degrees away from the dynamometer, as shown in Figure 6.

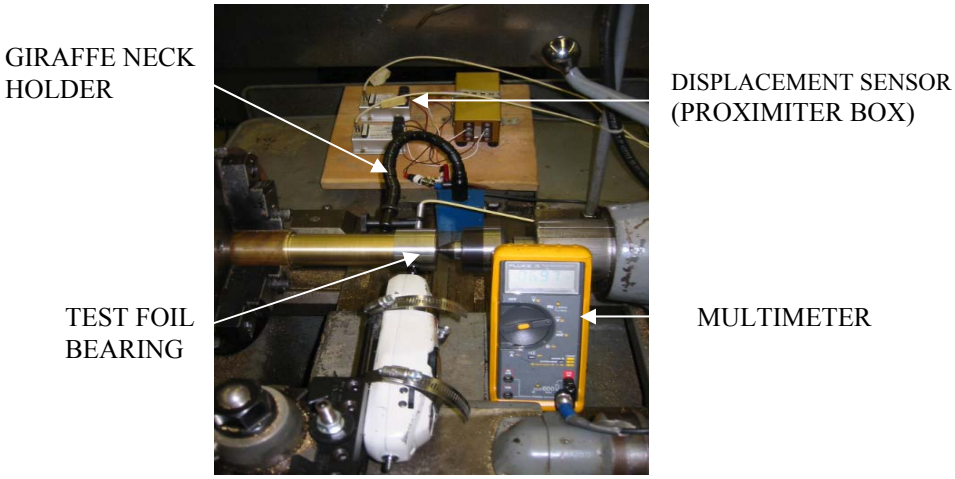

Figure 6 Test Setup for Static Experiments. Front View

The load application mechanism consists of moving the dynamometer horizontally toward the foil bearing sleeve. Once the dynamometer touches the bearing, the loading process starts from 0 lb. to 50 lb. The bearing deflections are quite peculiar at low loads (<10lb), and therefore more collection of data pairs (static load, bearing deflection) are taken at these loads. Notice that a reasonable time between individual loading processes is taken to ensure the reliability of the displacement data. The loading process is performed along eight angular positions 45 degrees apart from each other; each angular position is labeled as shown in Figure 7.

Note that the spot weld on the foil bearing is used as the reference angular coordinate (θ) and the angles are measured from the free end to the fixed end.

Structural characteristics can be distinguished from these experiments. Bearing deflection-versus-static load curves are plotted for CFBs 1 and 2. Deflection-versus-load curves corresponding to applied loads at opposite sides (180° spaced apart) of the bearing sleeve are grouped as paired measurements, i.e. positions 1 and 5 are displayed on the same curve. The bearing structural stiffness, therefore, is identified by taking the slope of the deflection(x)-versus-load curve (F) for each shaft diameter, i.e. $K = \partial F / \partial x$.

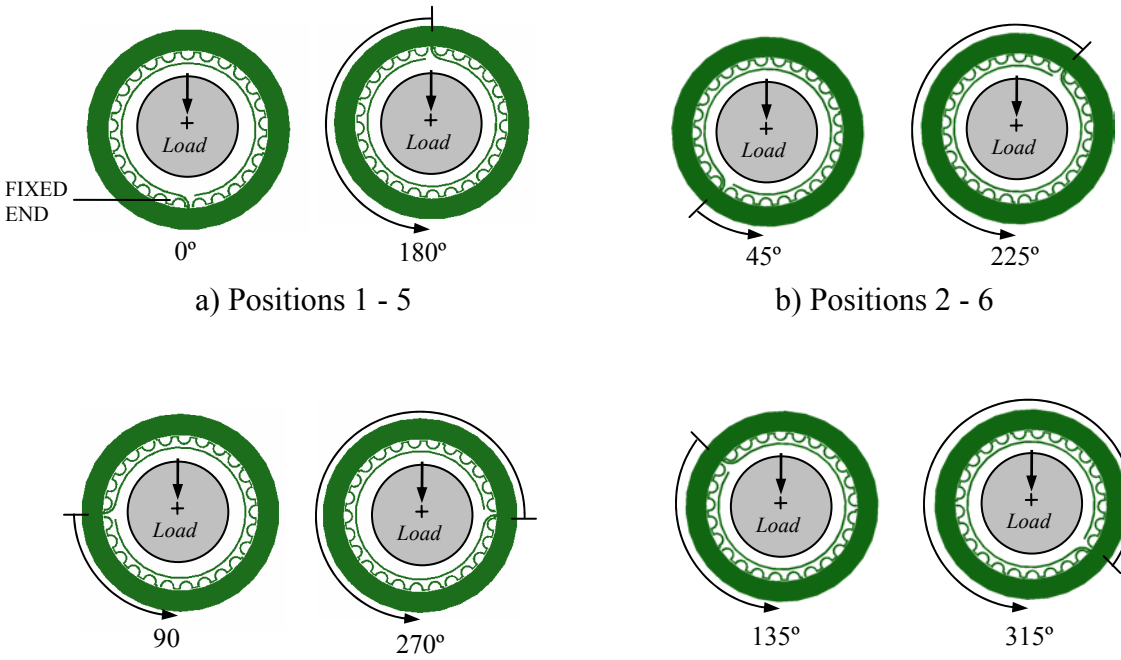

a) Positions 1 - 5 b) Positions 2 - 6

c) Positions 3 - 7 d) Positions 4 - 8

Figure 7 Labeled Angular Positions Grouped in Pairs

IV.2 EXPERIMENTAL RESULTS

Experimental results of foil bearing deflection versus static load for each particular configurations described above are obtained. Figures 8, 9 and 10 depict the structural deformation of CFB 1 when loaded at all angular positions and for the three different shaft diameters. Similar results are obtained for CFB 2, as shown in Figures 11, 12 and 13. Each figure displays bump foil deflection versus applied load for four test positions along meridional planes. The negative and positive values of static load do not indicate compression nor traction forces on the bearing. Figures 8 to 13 show a non linear relationship between bearing deflection and applied load. A polynomial curve fit establishes an analytical relation between the static load and the bearing deflection; i.e. $F = f(x)$. This relation is given by a third order polynomial and obtained for all pairs of angular orientations (see Figure 7). Recall that all tests results shown in Figures 8 to 13 are obtained using an eddy current sensor as the displacement sensor. Appendix B provides the results obtained with the dial gauge for shaft D_1 and comparison with the results obtained with an eddy current sensor.

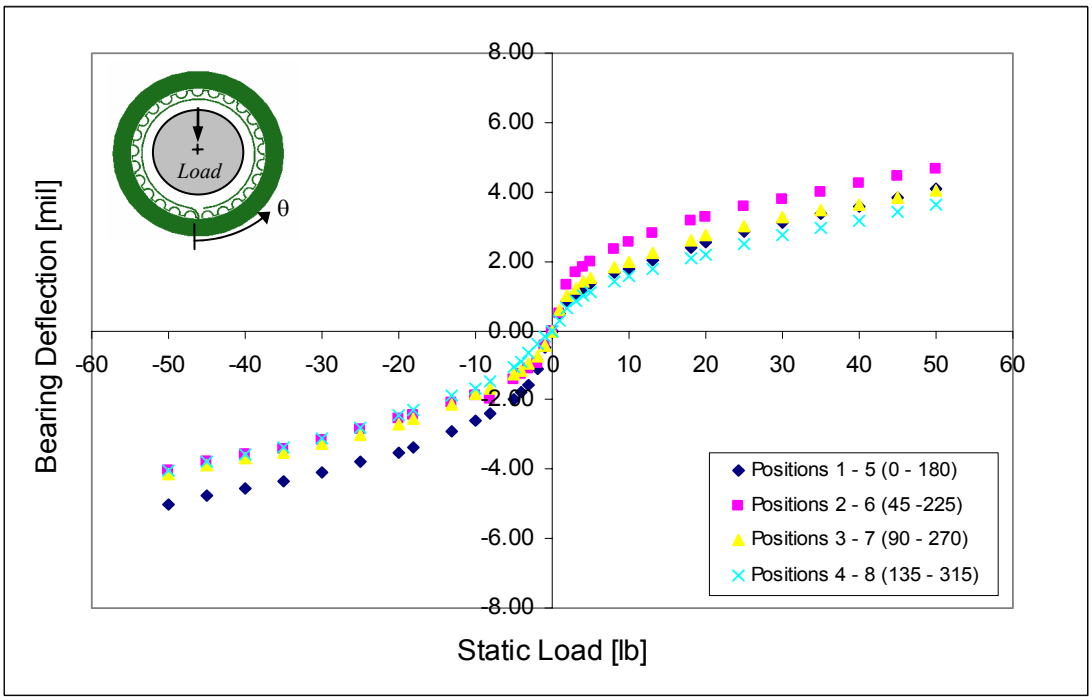

Figure 8 Deflection of CFB 1 versus Static Load for all Angular Positions (D_1 Shaft Diameter, 1.5 in. nominal)

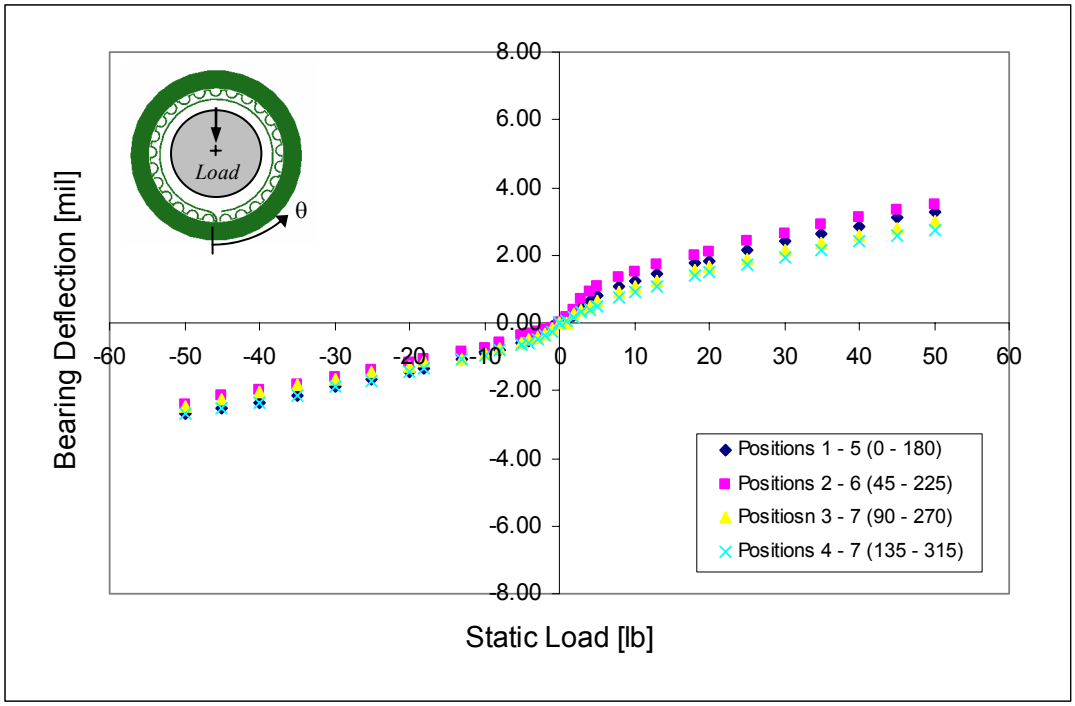

Figure 9 Deflection of CFB 1 versus Static Load for all Angular Positions (D_2 Shaft Diameter, 1.5 + 0.001 in)

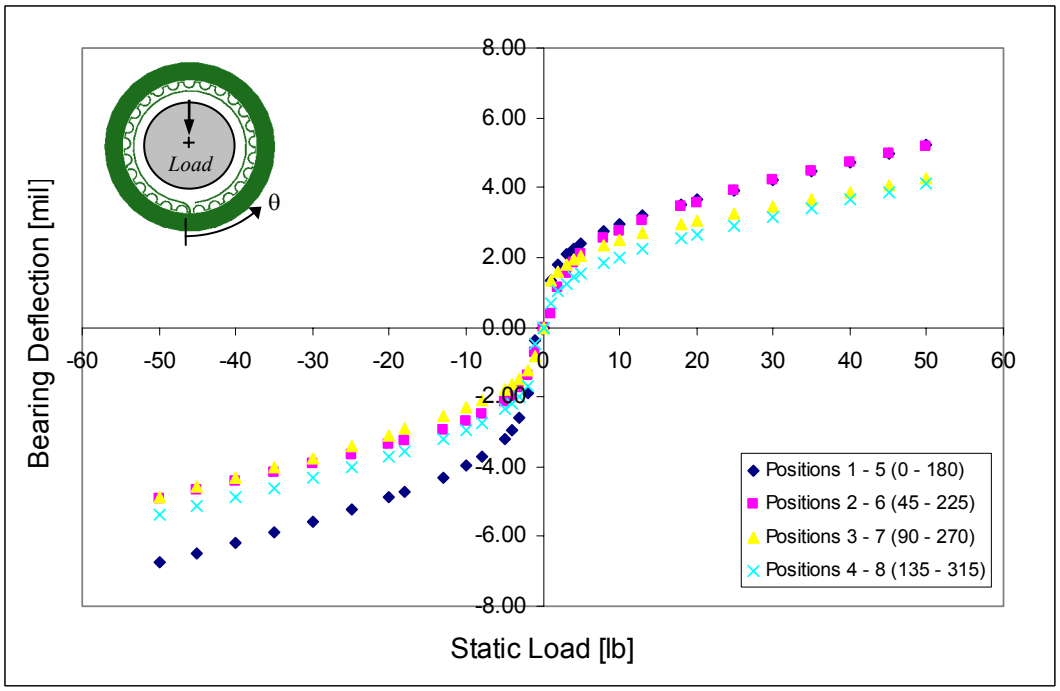

Figure 10 Deflection of CFB 1 versus Static Load for all Angular Positions (D_3 Shaft Diameter, 1.5 - 0.001 in)

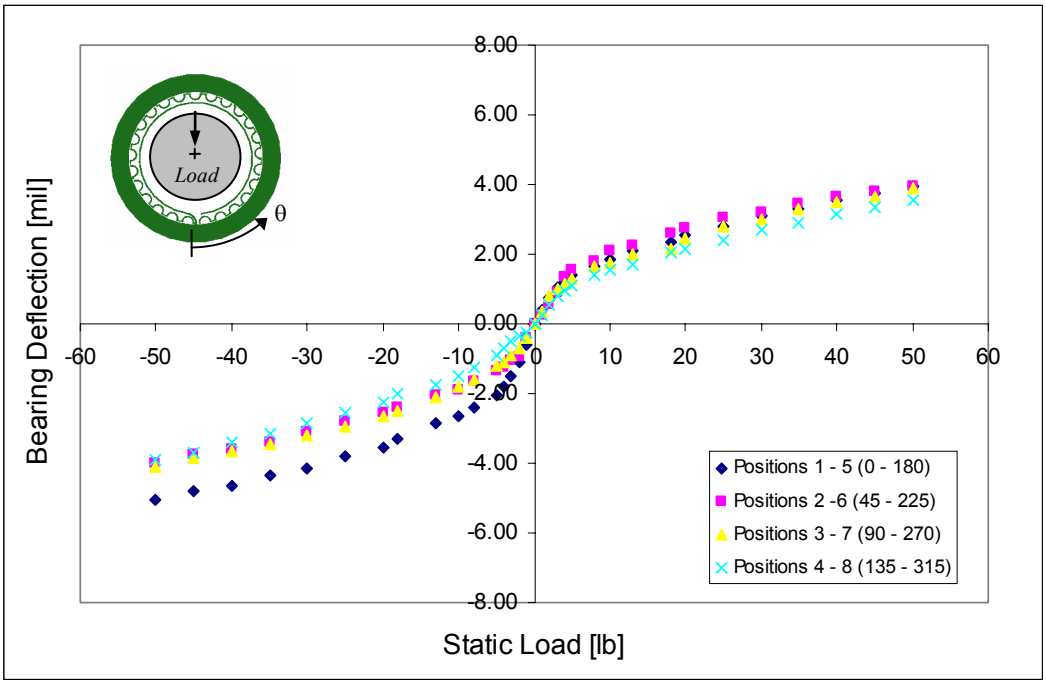

Figure 11 Deflection of CFB 2 versus Static Load for all Angular Positions (D_1 Shaft Diameter, 1.5 in. nominal)

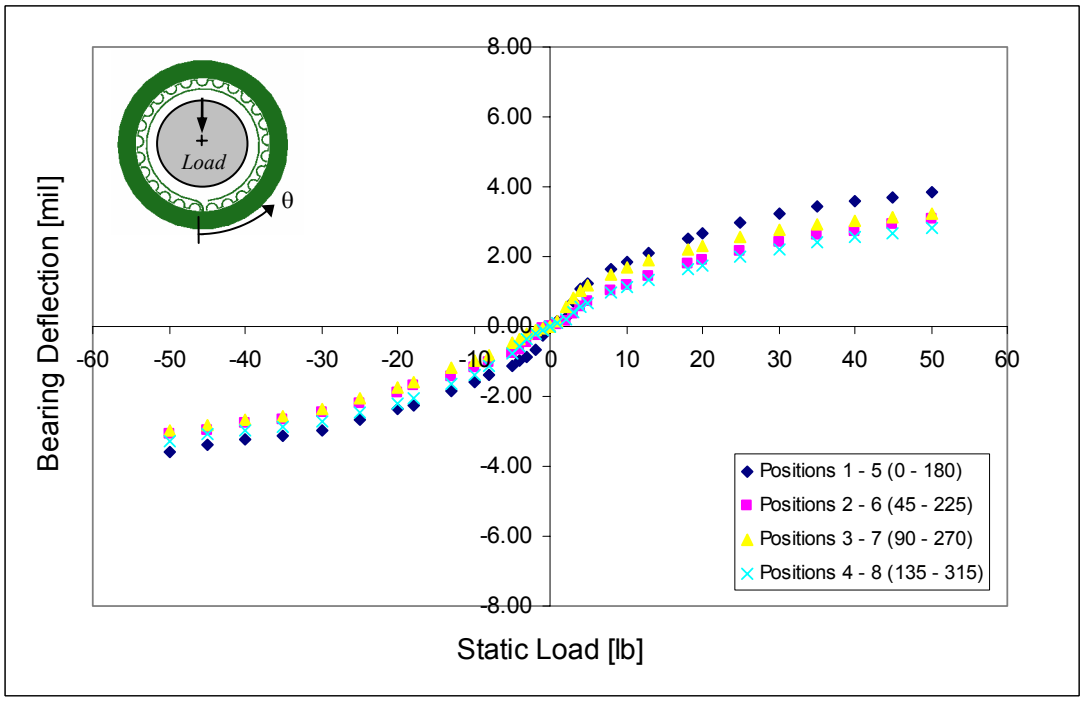

Figure 12 Deflection of CFB 2 versus Static Load for all Angular Positions (D_2 Shaft Diameter, 1.5 + 0.001 in)

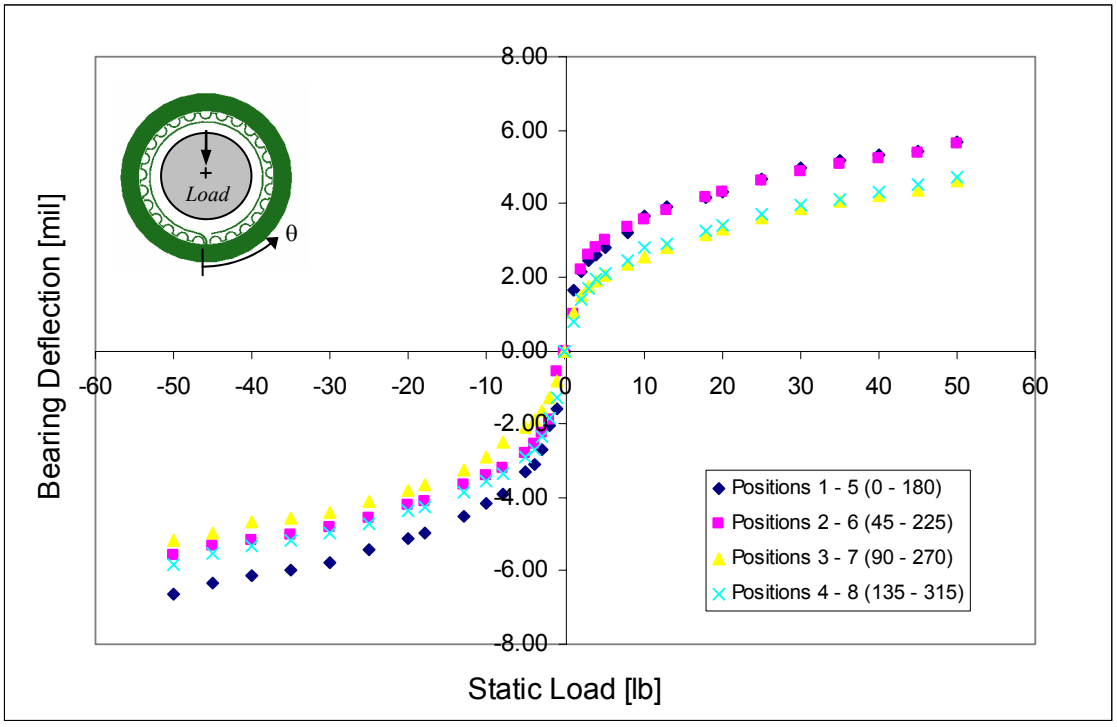

Figure 13 Deflection of CFB 2 versus Static Load for all Angular Positions (D_3 Shaft Diameter, 1.5 - 0.001 in)

The deformation structural mechanism of the foil bearings is clearly non linear as determined from the results. The foil bearing design introduces this non linear characteristic in the bump deformation process with respect to the applied load, therefore variable stiffnesses are achieved when the applied load changes. This non linear characteristic on the foil bearing deflection arises when the bearing starts being squeezing against the rigid shaft. At light static loads, only a few bumps are activated (compressed) due to the fact that the static load is not large enough to deform bumps far away from the position of static load application. The area of contact between the bearing and the shaft increases as the static load increases, therefore more bumps become activate. The bumps are positioned as parallel springs supporting the rigid shaft[6], and each time a bump stiffness becomes activated, the overall stiffness increases.

Table 2 shows the non linear (curvefits) polynomials, obtained from the measurements of the foil bearing deflection-versus-static load. Curve fit equations are given for CFB 1, at all angular positions and shaft diameters. Table 3 shows similar results for CFB 2.

Table 2 CFB1 Curve Fit Equations of Load-versus-Deflection for the Three Shaft Diameters.

Shaft Diameter	Angular Positions	Load F [lb] versus Deflection x [mil] Equations	x Range [mil]	Correlation Coefficient [7]
D_1 1.5 in	1 – 5 *(0° - 180°)*	$F = 0.436x^3+0.693x^2+ 2.764x$	[-5.00 , 4.10]	0.998
	2 – 6 (45° - 225°)	$F = 0.527x^3-0.555x^2+ 2.157x$	[-4.05 , 4.65]	0.998
	3 – 7 *(90° - 270°)*	$F = 0.571x^3+0.03x^2+ 2.99x$	[-4.15, 4.05]	0.998
	4 - 8 *(135° - 315°)*	$F = 0.565x^3+0.398x^2+5.265x$	[-4.05 , 3.65]	0.998
D_2 1.5+ 0.001 in	1 – 5	$F = 0.897x^3-1.106x^2+ 9.449x$	[-2.70 , 3.30]	0.998
	2 – 6	$F = 1.155x^3-2.699x^2+ 9.771x$	[-2.40 , 3.50]	0.993
	3 – 7	$F = 1.159x^3-1.454x^2+ 11.118x$	[-2.45 , 3.00]	0.995
	4 - 8	$F = 1.064x^3-0.124x^2+ 10.853x$	[-2.70 , 2.75]	0.998
D_3 1.5 - 0.001 in	1 – 5	$F = 0.237x^3+0.497x^2+ 0.720x$	[- 6.75, 5.20]	0.996
	2 – 6	$F = 0.360x^3-0.145x^2+ 1.213x$	[-4.90 , 5.15]	0.998
	3 – 7	$F = 0.480x^3+0.269x^2+ 1.615x$	[-4.85 , 4.25]	0.989
	4 - 8	$F = 0.418x^3+0.816x^2+ 2.237x$	[-5.40 , 4.10]	0.996

[6] Stiffness of spring in parallel ($K_t = K_1 + K_2 + K_3 + \ldots + K_n$)

[7] The correlation coefficient indicates the goodness of the curve fit to the test data.

Figures 8 through 13 depict the structural deformation of the foil bearings for various shaft diameters or bearing preload. No preload is induced with the shaft diameters D_1 and D_3, see Figures 8 and 10 for CFB1, and Figures 11 and 13 for CFB2. These figures show that the static load-versus-deflection curve at position 1 (negative values of position 1-5 curve) is particularly different from the results depicted for other angular positions. At position 1 (0º), the bearing is compressed toward the spot weld as depicted in Figure 7.a. Although results at position 1 show a different pattern, the deflection versus load still follows a cubic polynomial behavior.

Table 3 CFB2 Curve Fit Equations of Load- versus- Deflection for the Three Shaft Diameters.

Shaft Diameter	Angular Positions	Load F [lb] versus Deflection x [mil] Equations	x Range [mil]	Correlation Coefficient [8]
D_1 1.5 in	1 – 5 *(0º - 180º)*	$F = 0.449x^3+0.794x^2+ 2.761x$	[-5.05 , 3.95]	0.999
	2 – 6 (45º - 225º)	$F = 0.624x^3-0.071x^2+ 2.932x$	[-4.00 , 3.95]	0.998
	3 – 7 *(90º - 270º)*	$F = 0.561x^3+0.181x^2+ 3.959x$	[-4.10 , 3.90]	0.997
	4 - 8 *(135º - 315º)*	$F =0.555x^3+0.288x^2+ 6.109x$	[-3.90 , 3.55]	0.998
D_2 1.5+ 0.001 in	1 – 5	$F = 0.701x^3-0.361x^2+ 3.473x$	[-3.60 , 3.85]	0.998
	2 – 6	$F = 0.976x^3+0.059x^2+6.917x$	[-3.10 , 3.10]	0.999
	3 – 7	$F = 1.136x^3- 0.820x^2+ 5.055x$	[-2.95 , 3.25]	0.994
	4 - 8	$F = 1.129x^3+ 0.986x^2+ 6.104x$	[-3.30 , 2.80]	0.998
D_3 1.5 - 0.001 in	1 – 5	$F = 0.227x^3+ 0.274x^2 - 0.541x$	[-6.65 , 5.70]	0.998
	2 – 6	$F = 0.311x^3- 0.033x^2- 0.816x$	[-5.60 , 5.65]	0.999
	3 – 7	$F = 0.414x^3+ 0.324x^2+ 0.622x$	[-5.15 , 4.60]	0.999
	4 - 8	$F = 0.351x^3+ 0.54x^2+ 0.19x$	[-5.85 , 4.70]	0.999

At position 1(0º), the top foil and bumps around the spot weld of the bearing are being compressed towards the shaft as shown in Figure 14. The spot weld location denotes the fixed end of the foil strips. The bumps located at the free end, also shown in Figure 14, are less constrained than the bumps located at the fixed end. These last bumps are more constrained by the attachment at the spot weld and also by their neighboring bumps. The bearing sleeve, subjected to small loads applied at the location of the spot weld, tends to move toward the free end because the bumps located at this angular position provide less resilience to the movement

[8] The correlation coefficient indicates the goodness of the curve fit to the test data..

than the bumps located at the fixed end. Once the load increases, the bumps in the fixed end become active and the bearing develops higher stiffnesses.

The foil bearing structural stiffness is easily identified from the load versus deflection equations shown in Tables 2 and 3. Table 4 shows the derived structural stiffness equations for CFB1. Similar equations for CFB2 are shown in Table 5.

Table 4 CFB1 Derived Equations of Structural Stiffness -versus- Deflection for the Three Shaft Diameters

Shaft Diameter	Angular Positions	Structural Stiffness k [b/mil] versus Deflection x [mil] Equations	x Range [mil]
D_1 1.5 in	1 – 5 *(0° - 180°)*	$k = 1.308x^2+1.386\,x+ 2.764$	[-5.00 , 4.10]
	2 – 6 (45° - 225°)	$k = 1.695x^2+0.796x+5.265$	[-4.05 , 4.65]
	3 – 7 *(90° - 270°)*	$k = 1.581x^2-1.11x+ 2.157$	[-4.15, 4.05]
	4 - 8 *(135° - 315°)*	$k = 1.713x^2+0.06x+ 2.99$	[-4.05 , 3.65]
D_2 1.5+ 0.001 in	1 – 5	$k = 0.711x^2+0.994x+ 0.720$	[-2.70 , 3.30]
	2 – 6	$k = 1.08x^2-0.29x+ 1.213$	[-2.40 , 3.50]
	3 – 7	$k = 1.44x^2+0.538x+ 1.615$	[-2.45 , 3.00]
	4 - 8	$k = 1.254\,x^2+1.632x+ 2.237$	[-2.70 , 2.75]
D_3 1.5 - 0.001 in	1 – 5	$k = 2.691x^2-2.212x+ 9.449$	[- 6.75, 5.20]
	2 – 6	$k = 3.465x^2-5.398x+ 9.771$	[-4.90 , 5.15]
	3 – 7	$k = 3.477x^2-2.908x+ 11.118$	[-4.85 , 4.25]
	4 - 8	$k = 3.192x^2-0.224x+ 10.853$	[-5.40 , 4.10]

Table 5 CFB 2 Derived Equations of Structural Stiffness-versus-Deflection for the Three Shaft Diameters

Shaft Diameter	Angular Positions	Structural Stiffness k [b/mil] versus Deflection x [mil] Equations	x Range [mil]
D_1 1.5 in	1 – 5 *(0º - 180º)*	$k = 1.347x^2 + 1.588\,x + 2.761$	[-5.05 , 3.95]
	2 – 6 (45º - 225º)	$k = 1.872x^2 - 0.142x + 2.932$	[-4.00 , 3.95]
	3 – 7 *(90º - 270º)*	$k = 1.683x^2 + 0.362x + 3.959$	[-4.10 , 3.90]
	4 - 8 *(135º - 315º)*	$k = 1.665x^2 + 0.576x + 6.109$	[-3.90 , 3.55]
D_2 1.5+ 0.001 in	1 – 5	$k = 2.103x^2 - 0.722x + 3.473$	[-3.60 , 3.85]
	2 – 6	$k = 2.928x^2 + 0.118x + 6.917$	[-3.10 , 3.10]
	3 – 7	$k = 3.408x^2 - 1.64x + 5.055$	[-2.95 , 3.25]
	4 - 8	$k = 3.387x^2 + 1.972x + 6.104$	[-3.30 , 2.80]
D_3 1.5 - 0.001 in	1 – 5	$k = 0.681x^2 + 0.548x - 0.541$	[-6.65 , 5.70]
	2 – 6	$k = 0.933x^2 - 0.066x - 0.816$	[-5.60 , 5.65]
	3 – 7	$k = 1.242x^2 + 0.648x + 0.622$	[-5.15 , 4.60]
	4 - 8	$k = 1.053x^2 + 1.08x + 0.19$	[-5.85 , 4.70]

Note in Table 5, for D_3 shaft diameter, that for small bearing deflections the estimated stiffnesses are negative for positions 1-5 (0º - 180º) and 2-6 (45º - 225º). The negative stiffnesses arise due to the inaccuracy of the force versus deflection curve fit at light loads, although the force versus deflection curve fit accurately correlates the collection of data points (static load, bearing deflection) for the entire range of bearing deflections, as noted in Tables 2 and 3. As shown in Figure 14 for bearing deflections around ± 1 mil the curve fit follows a negative slope trend, which leads to negative stiffness values, as depicted in Figures 16 and 17 for CBF2. This inaccuracy on the structural stiffness at light loads, using a D_3 shaft diameter, yields into high values of stiffness uncertainty at light loads, i.e. the structural stiffness value (at -1 lb with a D_3 shaft diameter in Figure 18) is -0.541 lb/mil and its uncertainty is ± 0.615 lb/mil. However, once static loads and deflections increase, the stiffness uncertainty decreases. See uncertainty analysis in Appendix C.

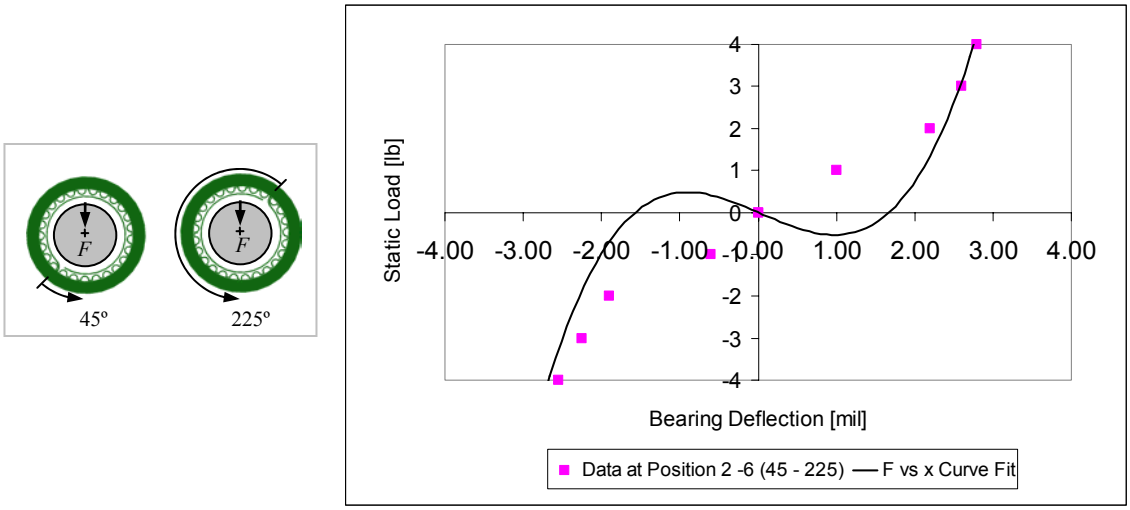

Figure 14 Static Load versus Bearing Deflection Curve Fit and Data at Low Loads for Position 2 - 6 (45º-225º). CFB2

The bump stiffnesses (K_1, K_2,..., K_{25}), shown in Figure 15, model the stiffness of each bump. The bump stiffness K_1 is likely to be smaller than bump stiffness K_{25}, since it is located at the free end. According to the description given above, the softer bump (K_1) is activated before the harder bump (K_{25}). Thus, at position 1 the bumps deflection is greater than at other angular positions, i.e. Table 6 shows that the rate of change of bump deflections for position 1 and position 5 are certainly different from each other at static loads from 0 lb to 5 lb. For light loads along position 1, the structural stiffness is practically given by the stiffness of the softest bumps alone. However, once the load increases, the hardest bumps provide more stiffness to the bearing, and then the rate of deflection of the bumps becomes smaller. Notice that preloading the bearing, as shown in Figures 9 and 12, eliminates the peculiar deformation behavior at position 1 (0º). The bearing preload expands the top foil and compresses the bumps before even the loading process starts. At position 1, the preload compresses the bumps at the free end sufficiently that when the loading process starts the bumps at both ends become active simultaneously.

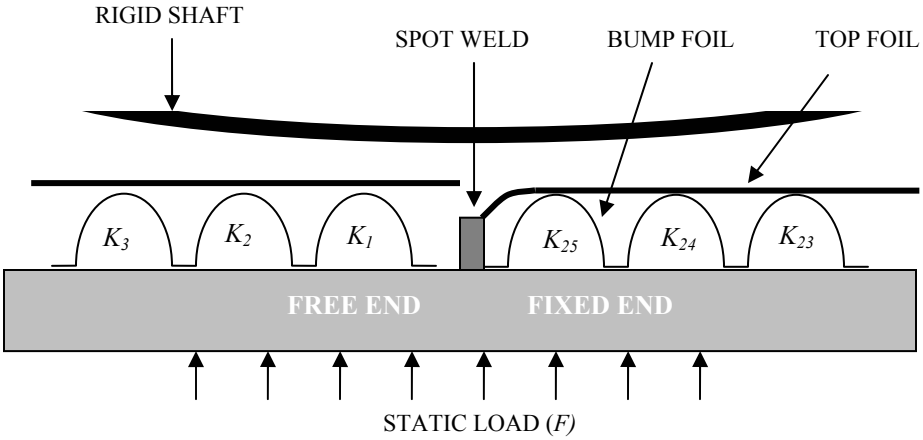

Figure 15 Schematic View of Bump Foils at Position 1 (0°)

Bearing structural stiffness curves versus deflection are obtained for all angular positions. Figures 16 and 18 depict the structural stiffness for the three shaft diameters; and corresponding to CBF1 and CFB2, respectively. Recall that the results are obtained using an eddy current sensor. Positions 2–6 (45°-225°) are displayed on the mentioned figures and remarkable differences are distinguished when using the different shaft diameters. Figures 17 and 19 show similar results for positions 1-5 (0°-180°). Foil bearing structural stiffness varies significantly with shaft diameter (preload), as shown in Figures 16 through 19. When the shaft diameter is D_3 (1.500-0.001 in), the bearing stiffness exhibits the widest curve and presents the lowest structural stiffness values. For the nominal shaft diameter D_1 (1.500 in), the bearing stiffness increases relative to the D_3 structural stiffness curve for any magnitude of bearing deflection. For shaft diameter D_2 (1.501 in), the structural stiffnesses reach the highest values.

The higher identified structural stiffnesses are obtained when the bearing is preloaded since the bumps are already compressed. Once the static load is increased high enough to overcome the opposite force, due to the preload; the bumps starts to compress further more towards the shaft. On the other hand, bearing deflection using a D_1 shaft nominal diameter is less constrained at light loads, and therefore its structural stiffness is smaller. In general, the identified structural stiffness versus bearing deflection curves along all angular positions, using the same shaft diameter, are quite similar. Significant differences are observed at position 1 (0) and when the bearing is not preloaded, see Figures 8, 10, 11, and 13. The measured deflection at position 2-5, 3-7, and 4-8 in the two CFBs and shaft diameters are approximately symmetrical about the vertical axis, with respect to the static load and bearing deflection.

Table 6 CFB1 Deflection at Positions 1 – 5 for D_1 Shaft Nominal Diameter

Static Load (lb)	*Angular Position 1*			*Angular Position 5*		
	Deflection [mil]	**Stiffness [lb/mil]**	**Uncertainty [lb/mil]** [9]	**Deflection [mil]**	**Stiffness [lb/mil]**	**Uncertainty [lb/mil]** [8]
0	0.00	2.765	0.210	0.00	2.765	0.513
1	0.50	3.785	0.165	0.50	2.400	0.961
2	0.85	4.888	0.210	1.10	2.825	1.048
3	1.05	5.663	0.228	1.55	3.763	0.904
4	1.20	6.313	0.248	1.80	4.513	0.840
5	1.35	7.021	0.266	2.00	5.231	0.803
8	1.65	8.615	0.306	2.40	6.981	0.756
10	1.80	9.500	0.329	2.60	8.013	0.746
20	2.55	14.811	0.420	3.50	13.954	0.731
25	2.85	17.347	0.456	3.80	16.405	0.744
30	3.10	19.641	0.489	4.10	19.092	0.755

[9] See General Uncertainty Analysis in Appendix C

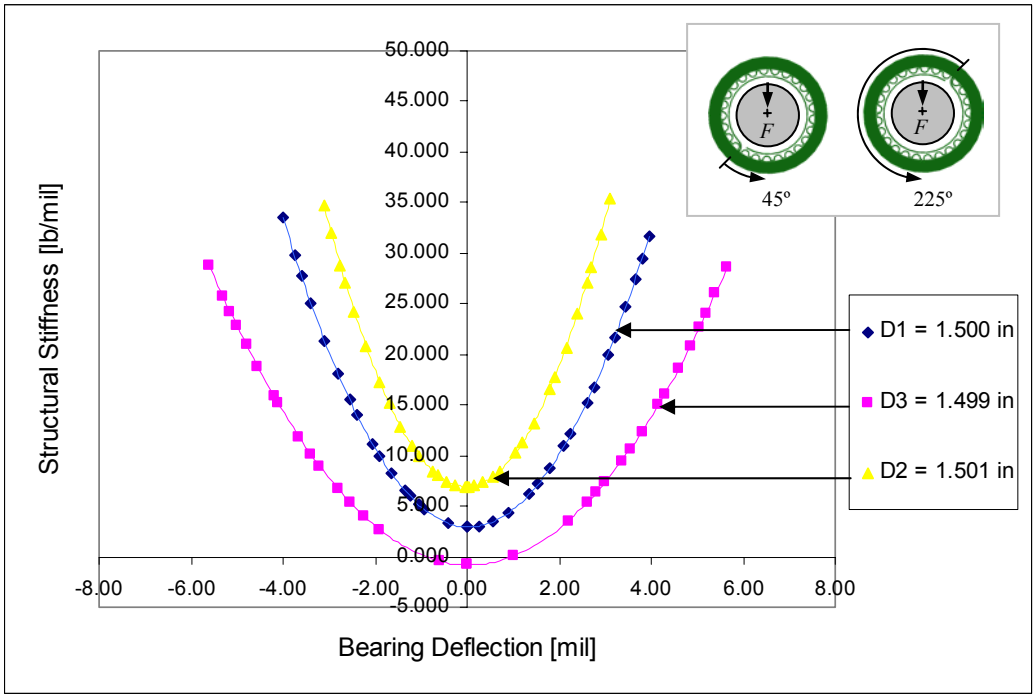

Figure 16 CFB2 Structural Stiffness versus Deflection for Three Shaft Diameters. Positions 2–6 (45° – 225°)

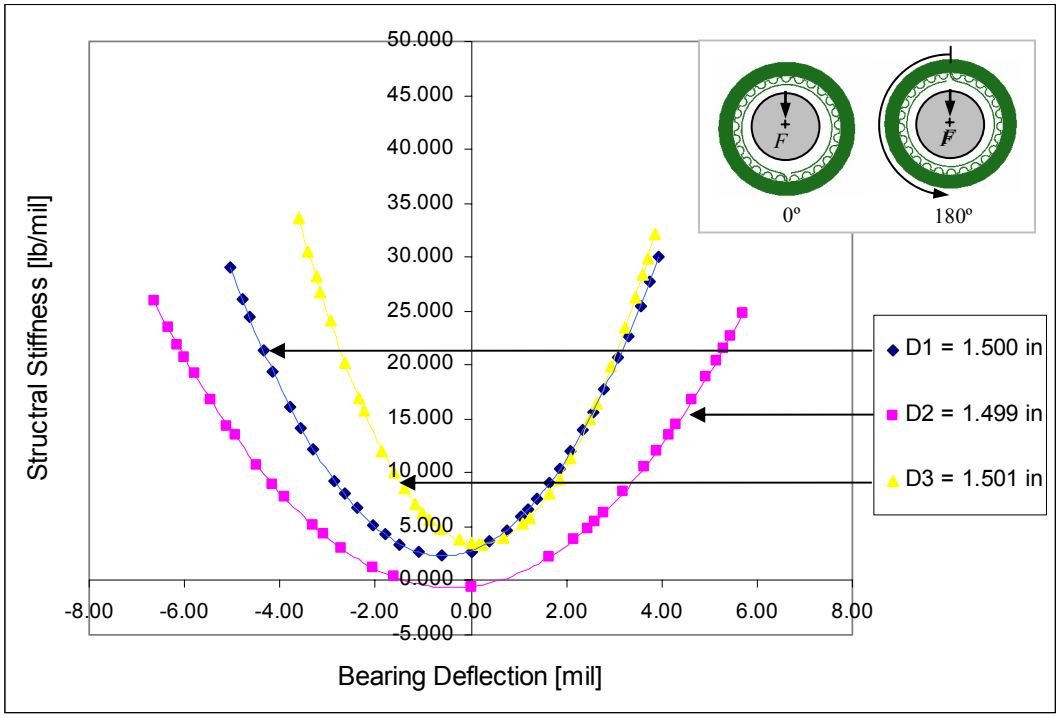

Figure 17 CFB2 Structural Stiffness versus Deflection for Three Shaft Diameters. Positions 1–5 (0° –180°)

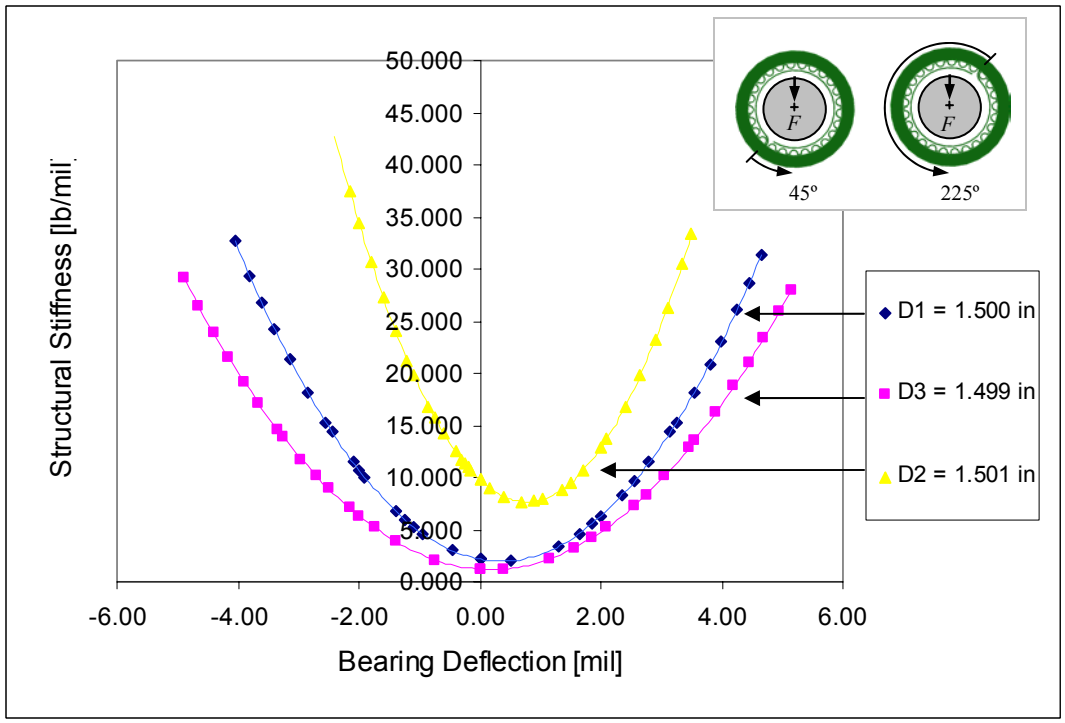

Figure 18 CFB1 Structural Stiffness versus Deflection for Three Shaft Diameters. Positions 2–6 (45° – 225°)

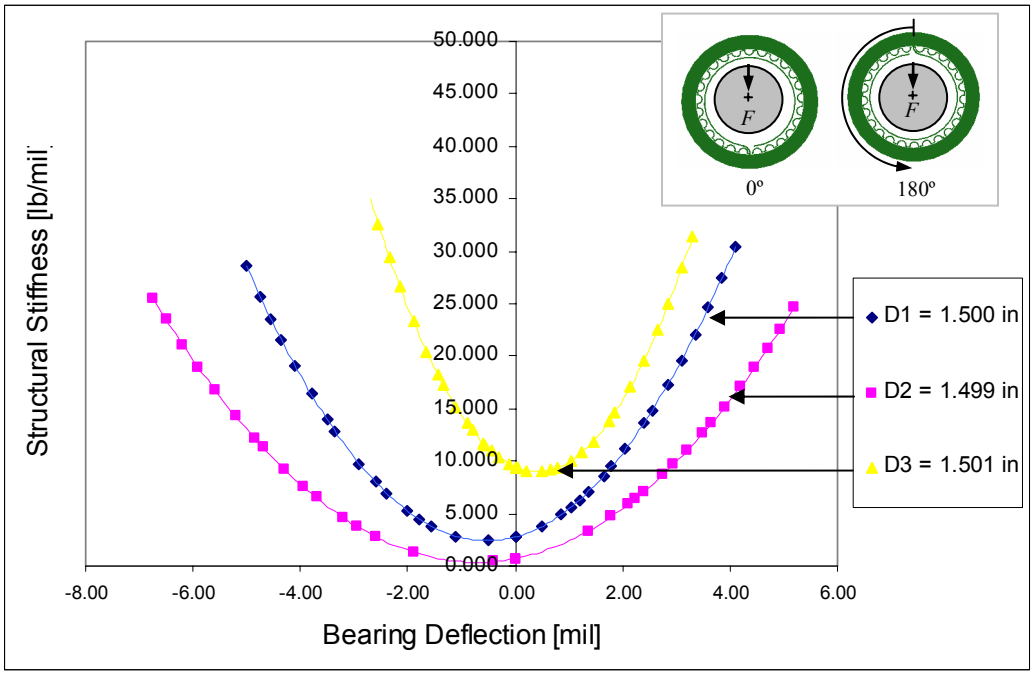

Figure 19 CFB1 Structural Stiffness versus Deflection for Three Shaft Diameters. Positions 1–5 (0° –180°)

Notice that the bearing structural stiffness is load dependant, as shown in Figures 21 and 22 for CFBs 1 and 2, respectively. Bumps gradually become activate as the static load increases (see Figure 20). When the static load increases, the rigid shaft in contact with the foil activates more bumps, therefore increasing the stiffness. Results shown in Figure 21 are for positions 4 – 8 (135°-315°) for CFB1. Similar results are obtained for CFB 2, as shown in Figure 22.

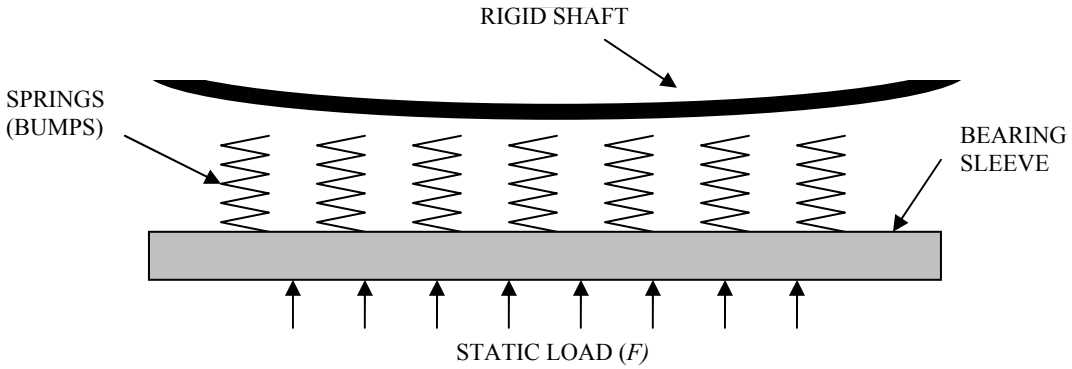

Figure 20 Schematic Representation of Bearing Structural Stiffening

Table 7 shows the maximum and minimum values of bearing structural stiffness at each angular position for the three shaft diameters. Maximum and minimum structural stiffness are identified at maximum and minimum static loads, respectively. The reported values of maximum and minimum stiffness are obtained using equations in Table 4 for CFB1.

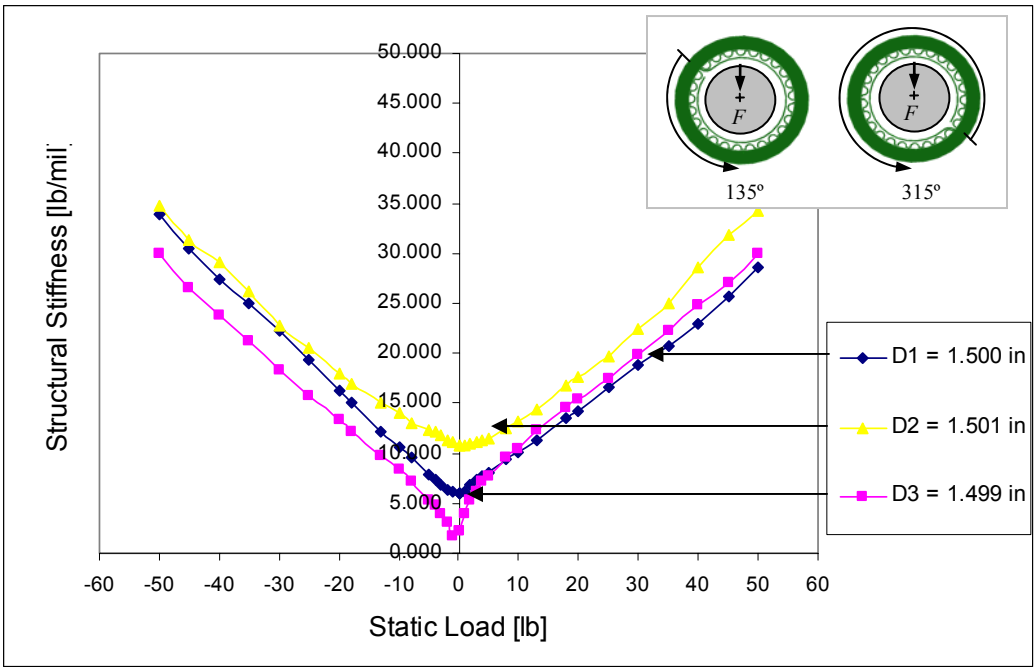

Figure 21 Linear Behavior of CFB1 Structural Stiffness versus Load with Three Shaft Diameters. Positions 4 – 8 (135°-315°)

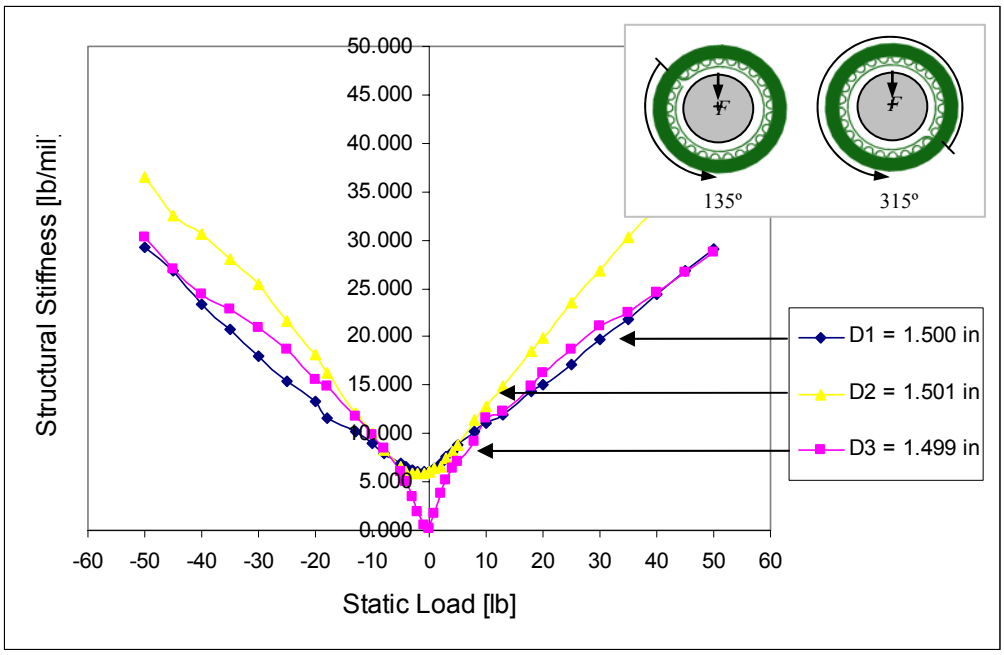

Figure 22 Linear Behavior of CFB2 Structural Stiffness versus Load with Three Shaft Diameters. Positions 4 – 8 (135°-315°)

Table 7 Maximum and Minimum CFB1 Structural Stiffness for the Three Shaft Diameters

Shaft Diameter	Angular Positions	Maximum Structural Stiffness [lb/mil]	Minimum Structural Stiffness [lb/mil]
D_1 1.5 in	1 – 5 *(0° - 180°)*	30.45	2.75
	2 – 6 (45° - 225°)	32.65	2.15
	3 – 7 *(90° - 270°)*	32.25	2.99
	4 – 8 *(135° - 315°)*	33.84	6.06
D_2 1.5+ 0.001 in	1 – 5	34.61	9.47
	2 – 6	39.45	9.97
	3 – 7	39.27	11.12
	4 - 8	35.52	10.89
D_3 1.5 - 0.001 in	1 – 5	26.06	0.68
	2 – 6	29.10	1.21
	3 – 7	32.51	1.45
	4 - 8	30.57	2.22

Figures 23 and 24 show the foil bearing stiffness for all angular positions and for CFB1 and CFB2, respectively. Structural stiffness is shown for two loads (50 lb and 5 lb) and the three shaft diameters. The use of different shaft diameters renders significant differences on the structural stiffnesses throughout the load span. Though, as mentioned before, the bearing preload (D_2) produces the highest structural stiffness at light loads due to the small bump deflections, see Figures 23 and 24 where the D_2 stiffness curve (at light loads) is always above the others. Note that structural stiffnesses when shaft diameter is D_3 are the lowest at any static load, the influence on the initial gap between the bearing and the shaft spanning throughout the whole load range. Recall that Figure 23 displays results for CFB1 and Figure 24 for CFB2.

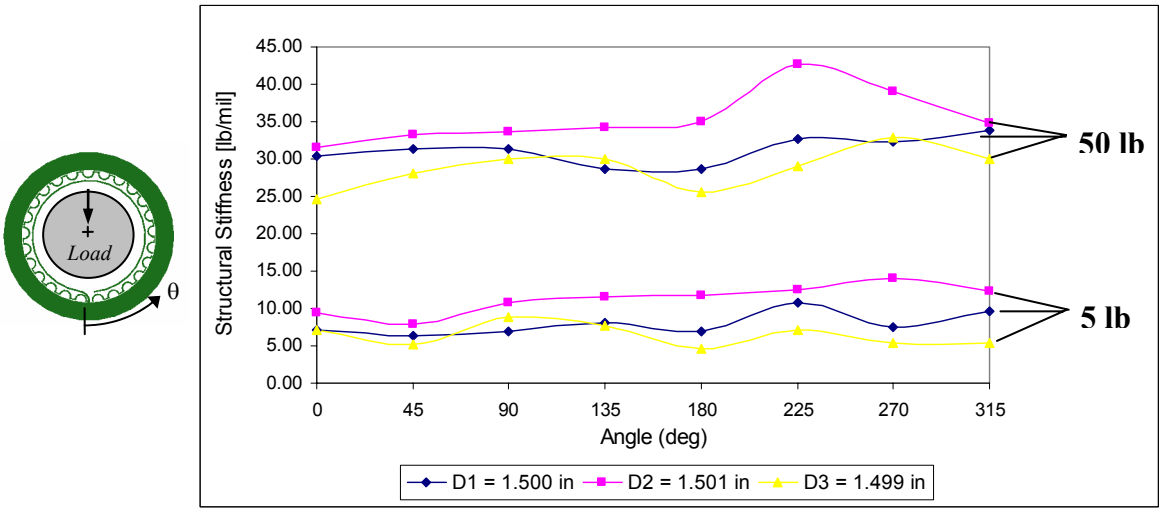

Figure 23 Identified CFB1 Structural Stiffness at all Angular Positions under Two Static Loads, 50 lb and 5 lb. (See Table 5 to Identify each Angular Position)

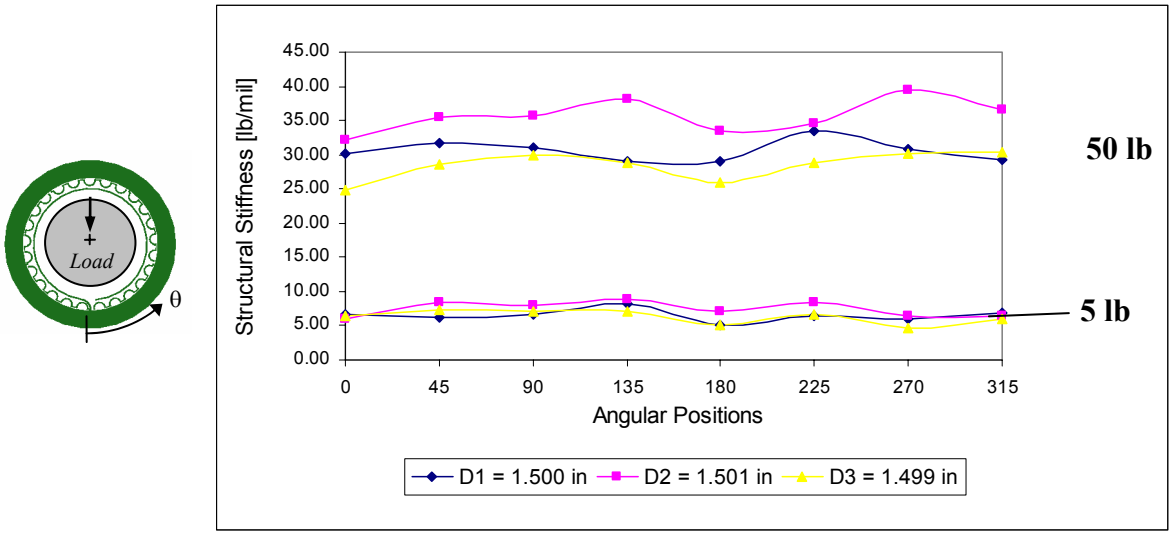

Figure 24 Identified CFB2 Structural Stiffness at all Angular Positions under Two Static Loads, 50 lb and 5 lb. (See Table 5 to Identify each Angular Position)

Tables 8 and 9 show the bearing preload effect on the structural stiffness for CFB1 and CFB2, respectively. A structural stiffness average (K_A) at each angular position is calculated for each shaft diameters. The highest structural stiffness average in both bearings is identified when the bearing is preloaded (D_2), i.e. for 50 lb and 5 lb the K_A is 35.55 lb/mil and 11.28 lb/mil, respectively (see Table 8). A similar finding is identified for CFB2 (see Table 9). An overall stiffness average (K_{OA}) is also obtained from the individual structural stiffness average (K_A) of each shaft diameters. The standard error of an estimate (*SEE*) is calculated to evaluate the goodness of the structural stiffness average and the overall stiffness average. The highest *SEE* percentages are observed at 5 lb for both bearings, as seen in Table 8 and 9.

Table 8 CFB1 Structural Stiffness Averages for all Angular Positions and their Standard Deviation

Angular Positions	Structural Bearing Stiffness [lb/mil]					
	50 lb			5 lb		
	D_1	D_2	D_3	D_1	D_2	D_3
1 (0°)	30.45	31.46	24.61	7.02	9.40	7.10
2 (45°)	31.28	33.32	28.01	6.27	7.92	5.19
3 (90°)	31.35	33.68	29.93	6.94	10.70	8.77
4 (135°)	28.63	34.31	29.99	8.11	11.53	7.78
5 (180°)	28.57	35.04	25.51	6.98	11.74	4.61
6 (225°)	32.66	42.69	29.10	10.71	12.49	7.04
7 (270°)	32.26	39.11	32.91	7.56	14.11	5.32
8 (315°)	33.84	34.79	29.96	9.62	12.36	5.32
K_A [lb/mil]	31.13	35.55	28.75	7.90	11.28	6.39
SEE [lb/mil]	2.01	3.90	2.89	1.65	2.08	1.60
% *SEE*	6.47	10.96	10.04	20.82	18.47	25.06
Overall K_{OA} [lb/mil]		31.81			8.53	
Overall *SEE* [lb/mil]		2.82			2.04	
Overall % *SEE*		8.86			23.98	

Table 9 CFB2 Structural Stiffness Averages for all Angular Positions and their Standard Deviation

Angular Positions	Structural Bearing Stiffness [lb/mil]					
	50 lb			5 lb		
	D_1	D_2	D_3	D_1	D_2	D_3
1 (0°)	30.05	32.13	24.73	6.61	5.88	6.34
2 (45°)	31.60	35.41	28.56	6.15	8.43	7.37
3 (90°)	30.98	35.71	29.86	6.60	7.99	7.16
4 (135°)	29.15	38.19	28.80	8.16	8.82	7.16
5 (180°)	29.10	33.55	25.96	5.17	7.11	5.07
6 (225°)	33.47	34.68	28.79	6.54	8.48	6.68
7 (270°)	30.78	39.54	30.20	5.95	6.48	4.74
8 (315°)	29.21	36.51	30.33	6.94	6.53	6.02
K_A [lb/mil]	30.54	35.72	28.40	6.51	7.47	6.32
SEE [lb/mil]	1.63	2.59	2.19	0.93	1.19	1.07
% *SEE*	5.34	7.24	7.73	14.25	15.97	16.86
Overall K_A [lb/mil]	31.55			6.77		
Overall *SEE* [lb/mil]	3.07			0.50		
Overall % *SEE*	9.73			7.41		

Figures 23 and 24, and Tables 8 and 9 facilitate a comparison between the stiffnesses for bearings CFB1 and CFB2. In general both foil bearings present similar structural characteristics throughout all angular positions and using the three shaft diameters. However as seen in Tables 8 and 9, CFB2 has a smoother stiffness behavior at light loads along all angular positions than CB1, i.e. the Overall *SEE* percentage for CFB2 is 7.41 % while for the CFB1 is 23.98 %. At high loads both bearings act similar with respect to the angular positions.

In addition to the foil bearing structural stiffness, the hysteresis in a foil bearing is also a relevant structural characteristic because it provides information about the damping mechanism. To identify such behavior the foil bearings are loaded and unloaded in the same set of measurements. Therefore, information about the foil bearing structural damping is provided depending on the loading and unloading paths. Previous results by Ku et al. [4, 8] and Heshmat

[9] show an evident structural hysteresis when loading and unloading the bump foils. Heshmat [5] explains that this phenomenon plays a major role in enhancing the bearing damping capability. Ku et al. [4] illustrate this hysteretic phenomenon as a product of Coulomb damping inherent to foil bearings. According to [10], Coulomb damping or dry friction is produced from two sliding surfaces rubbing against each other. Hence, Coulomb damping in foil bearings is produced by the sliding between the top foil and the bump foils while in contact, and also by the bump foils and the bearing sleeve, see Figure 25.

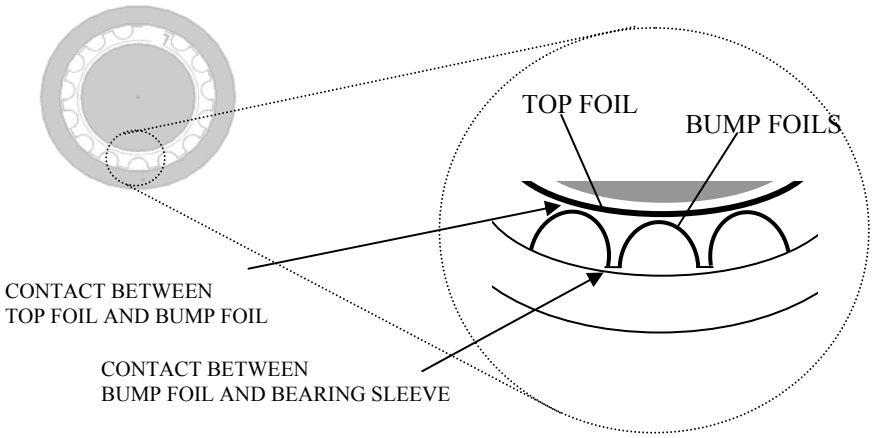

Figure 25 Schematic View of Coulomb Damping Source in Foil Bearings

Experiments of loading and unloading compliant foil bearing CFB1 are shown in Figure 26, for angular positions 1 – 5. Friction forces between the foil surfaces restrain the movement of the bump foil and the top foil when the bearing is being unloaded; therefore the unloading path follows different direction than the loading path.

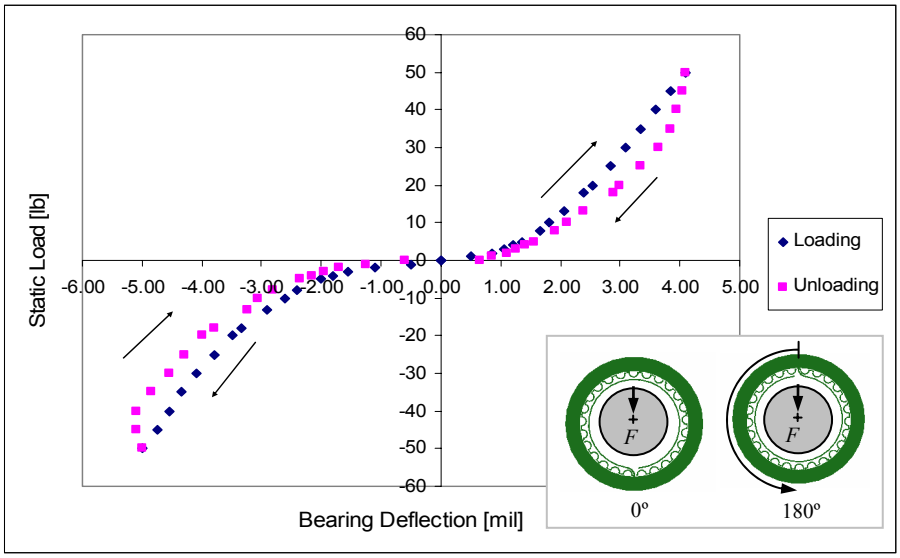

Figure 26 Hysteretic Phenomenon on CFB1 for Position 1 – 5 and Using a D_1 Shaft Nominal Diameter

V. PREDICTION OF FOIL BEARING STIFFNESS

Analytical approaches to predict foil bearing structural stiffness have been developed throughout the last 15 years. Ku et al. [2] develop a model for predicting bump-foil strip deformation and its equivalent structural stiffness and viscous damping coefficients. This model takes into account the interaction of adjacent bumps and the friction forces present in foil bearings. Iordanoff [5] develops a more simplistic model and provides the structural stiffness of a single bump for two different cases, i.e. one with a fixed end and one with both ends free.

The analysis predicts the foil bearing structural stiffness accounting for the influence of each bump and, including the dry friction coefficient, and radial position of the applied load. Note that Iordanoff's formulae [5] are utilized for estimating the individual bumps structural stiffness. In conducting the analysis, the bump pitch (p) is assumed to be constant and the interaction between bumps is neglected.

The structural stiffness for a one end welded bump (K_W) and a free ends bump (K_F) are given by [5]

$$K_W = \frac{F}{\delta} = \frac{E \cdot t^3 \cdot \sin^3\left(\alpha/2\right)}{12 \cdot {l_o}^3 \cdot p \cdot J(\alpha) \cdot \left(1-\upsilon_P^2\right) \cdot p \cdot L} \tag{1}$$

$$K_F = \frac{F}{\delta} = \frac{E \cdot t^3 \cdot \sin^3\left(\alpha/2\right)}{6 \cdot {l_o}^3 \cdot p \cdot l(\alpha) \cdot \left(1-\upsilon_P^2\right) \cdot p \cdot L} \tag{2}$$

where (E, υ) are the material elastic modulus and Poisson ratio, respectively; ($p_x L$) is the projected area of the top foil, $J(\alpha)$ and $I(\alpha)$ are function of α and the dry coefficient (μ_f), p is the bump pitch, t is the foil thickness, h is the bump height, δ is the bump deflection, $2_x l_o$ represents the bump length, F is the applied load and α is the bump arc angle. Figure 27 shows the parameters of importance.

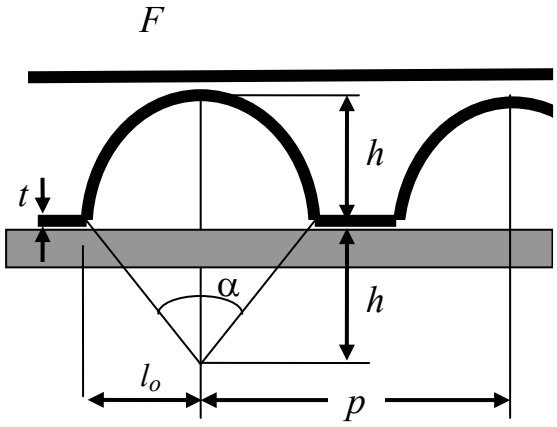

Figure 27 Bump Dimensional Parameters for Single Bump Stiffness Approximation

V.1 FOIL BEARING STRUCTURAL STIFFNESS MODEL

The analysis for approximating foil bearing stiffness requires the modeling of the structural stiffness of each bump along all angular positions. The bump stiffness model mainly depends on the bump configuration. As mentioned before, test foil bearings have twenty five bumps which are separated into five pads, each one with five bumps. Each pad is welded at one end and free at the other (see Figure 4). Therefore, the structural stiffness of each bump is determined by its location along the angular positions, i.e. fixed end or free end. The test foil bearings are also distinguished by the spot weld, which spans approximately 10 degrees along the bearing sleeve. Although the spot weld attaches one pad to the bearing sleeve, it does not follow the same configuration as the weld lines. The spot weld also attaches the top foil at one end to the bearing sleeve; therefore, it leaves a gap between both ends of the top foil. These bump configurations lead into a bump stiffness model as the one shown in Figure 28.

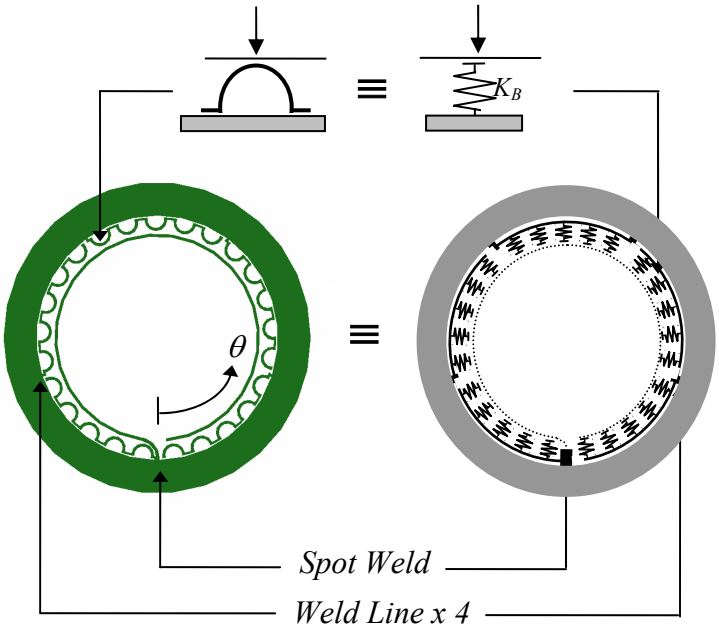

Figure 28 Equivalent Foil Structural Stiffness Model

The foil bearing structural stiffness model represents the bumps as springs whose stiffnesses are known. The structural stiffness of the bump next to the spot weld and the weld lines is estimated with Equation (1), while the rest of the bump stiffnesses are estimated using Equation (2). However, the bump next to the fixed bump at the spot weld has an intermediate stiffness (K_I). The stiffness of this bump is interpolated between the stiffness of the free end and the fixed end in order to have a smoother stiffness transition at the spot weld.

Figure 29 shows the structural stiffness distribution along all angular positions for the structural stiffness model explained above. Note that every five bumps the structural stiffness increases due to the welded bump constrain, and also notice that the stiffness distribution is obtained from the nominal dimensions of the foil bearing, see Table 1. Recall that the angular location of each bump is measured from the free end to the fixed end, i.e. 0° represents the free end and 350° represents the fixed end.

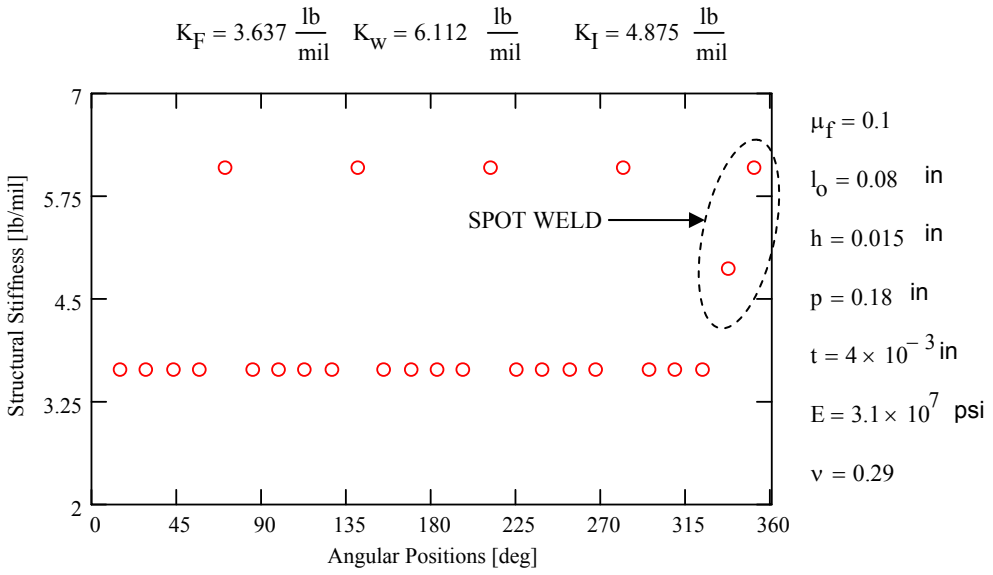

Figure 29 Structural Stiffness Distribution for Each Bump Throughout all Angular Positions. ($\mu_f = 0.1$; Nominal Foil Bearing Dimensions)

The bump structural stiffness model is sensitive to several foil bearing dimensional parameters, see Equations (1) and (2). The selection of these parameters is based on the information given by the foil bearing manufacturer (Table 1). However, it is important to evaluate the influence of these parameters over the bump stiffness model to assure the accuracy of the analytical results. Hence, Figure 30 shows the predicted single bump stiffness as a function of the dry friction coefficient. The structural bump stiffness increases as the friction coefficient rises. Note that for high friction coefficients (approximately $\mu > 0.5$), the structural stiffness increases dramatically leading into bump locking.

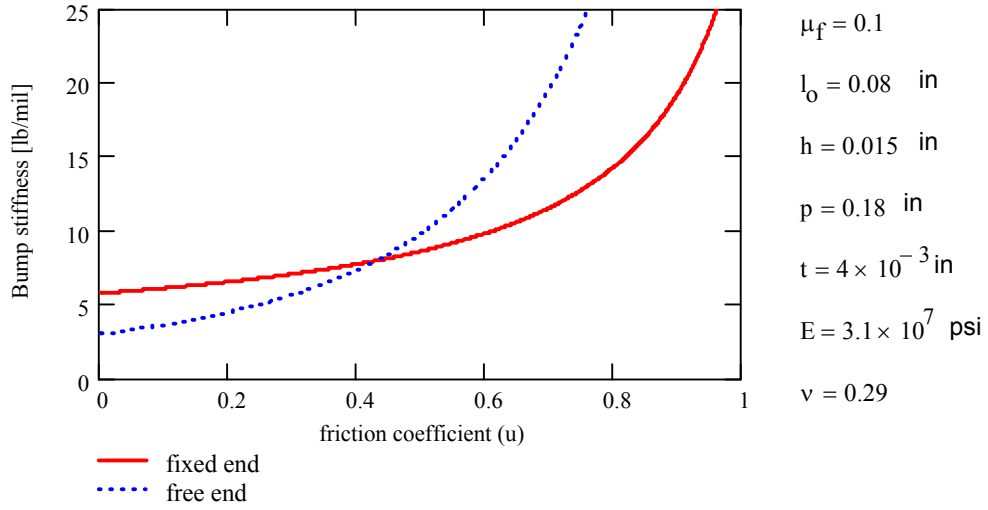

Figure 30 Predicted Structural Stiffness of a Single Bump for Different Dry Friction Coefficients. Nominal Foil Bearing Dimensions

Figures 31 and 32 show the bump stiffnesses as a function of changes in the bump height (h) and bump length ($2_x l_o$), respectively. Notice that the bump height is evaluated over a range of ± 40 % of its nominal value, i.e. h = 0.015 in.; while the half bump length is evaluated over a range of ± 10% of its nominal value, i.e. l_o = 0.008 in. All other parameters are noted in the figures. Appendix D contains the formulae for evaluating the structural stiffness of a single bump.

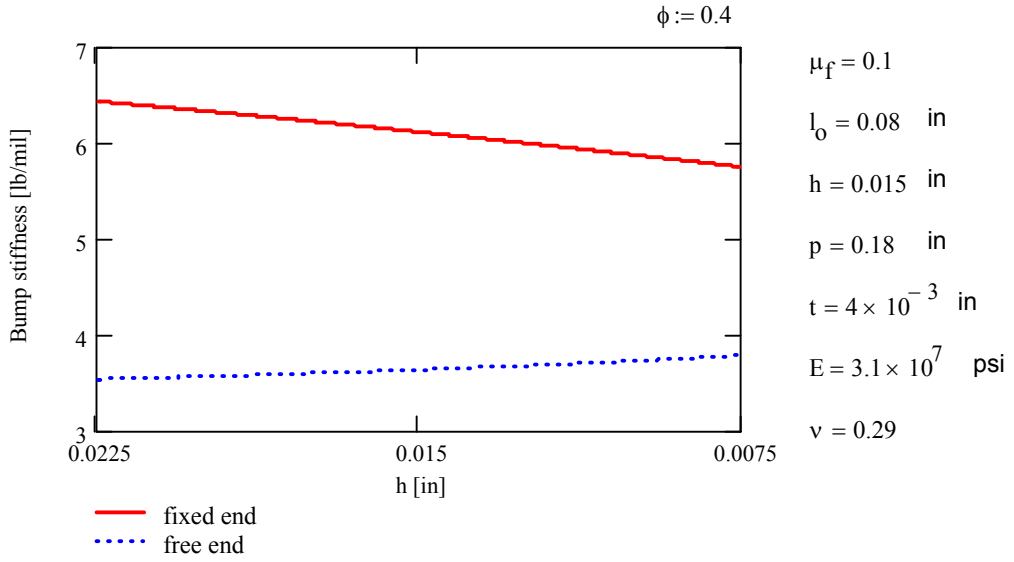

Figure 31 Predicted Structural Stiffness of a Single Bump for a ± 30% Range of the Nominal Bump Height. (μ_f = 0.1; Nominal Foil Bearing Dimensions)

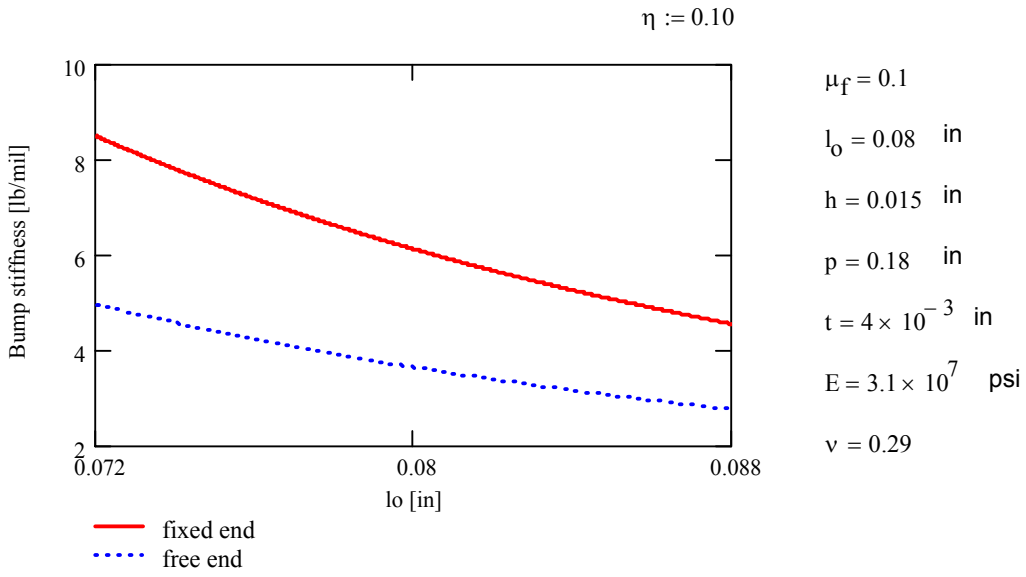

Figure 32 Predicted Structural Stiffness of a Single Bump for a ± 10% Range of the Nominal Half Bump Length. (μ_f = 0.1; Nominal Foil Bearing Dimensions)

Figure 31 illustrates that variations of 40% of the nominal bump height produces little changes in the bump stiffness, i.e. at the maximum bump height variation (40%) the bump

stiffness for the fixed end is 6.432 lb/mil while the bump nominal stiffness is 6.112 lb/mil. Therefore, the bump stiffness has a maximum bump stiffness variation of approximately 5.7% of the nominal bump stiffness when the nominal bump height is selected to vary ± 40%. Notice that 40% of the bump height represents approximately the maximum bearing deflection reported in the experimental results, i.e. 6 mil. In general, the variation of the structural stiffness with respect to the bump height seems linear for the selected bump height range.

On the other hand, the bump length ($2_x l_o$) leads to a stronger dependency of the bump structural stiffness, as shown in Figure 32. The selected range of 10 % of the nominal bump length is chosen based on the bump height range, i.e. 40%. Since the ratio between the bump length ($2_x l_o$) and the bump height (h) is significantly large, then a certain percentage of bump height variation yields in small percentages of the bump length variations, i.e. a variation of 100% on the bump height produces a variation of 13% on the bump length[10]. Thought, as seen in Figure 32, the bump stiffness changes significantly with a 10% variation of the bump length, i.e. at the maximum bump length variation (10%), the bump stiffness for the fixed end is 8.46 lb/mil while the bump nominal stiffness (0%) is 6.11 lb/mil. Therefore, the bump stiffness has a maximum bump stiffness variation of approximately 38.7% for bump lengths ($2_x l_o$) varying ± 10% around its nominal value.

Thus, the friction coefficient (μ_f) and the bump length ($2_x l_o$) are the two most sensitive parameters for estimation of bump stiffness.

The analytical procedure to determine foil bearing structural characteristic relies on the identification of the reaction forces produced by the bumps based upon three parameters: nominal clearance (c_{nom}), radial preload (r) and range of rotor displacements. Figure 33 shows the coordinate systems on the foil bearing and used for determining the reaction forces. The (X, Y) system represents the rotor displacement in the vertical and horizontal direction, being the X axis the spot weld; and the (ζ-η) system represents the normal and transverse deflection of each bump, respectively.

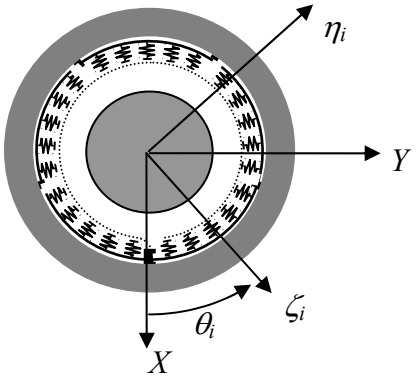

Figure 33 Coordinate Systems in the CFB for Prediction of Bearing Stiffness

[10] Based on the ellipse perimeter formula.

The normal deflection of each bump (ζ_i), taking into account the bearing preload and the nominal clearance, is given by

$$\zeta_i = X \cdot \cos(\theta_i) + Y \cdot \sin(\theta_i) + r - c_{nom} \tag{3}$$

where X and Y are the rotor displacements along the *(X, Y)* axes.

Equation (3) shows the deflection of each bump for a given rotor displacement, bearing preload (r) and nominal clearance (c_{nom}). In general, the bump deflection is calculated for three different bearing preloads, i.e. r = 0, r = 0.5 mil, and r = - 0.5 mil, to facilitate the comparison between the predicted and experimental results using the three different shaft diameters. On the other hand, the rotor displacement is selected from the maximum bearing deflection obtained on the static tests. According to the foil bearing manufacturer, the nominal radial clearance for a 1.500 in. shaft diameter is 0.0014 in.

Once the bump deflections are predicted, the reaction forces (F_ζ) are calculated for each bump.

$$F_{\zeta_i} = K_B(H_i) \cdot \zeta_i \quad \text{if } \zeta_i < 0 \tag{4}$$

where K_B is the predicted bump stiffness, and $H_i = h - \zeta_i$ is the actual bump height

Note that the bump stiffness (K_B) depends on the location of the bump along the foil bearing, i.e. fixed end or free end. The overall foil bearing reaction forces along the direction of the applied load, (β), is determined by;

$$F_{\zeta_i} = F_{X\,i} \cdot \cos(\beta) + F_{Y\,i} \cdot \sin(\beta) \tag{5}$$

where, β is the direction of the applied load, and F_X and F_Y are

$$F_{X_i} = \sum_{i=1}^{N} F_{\zeta\,i} \cdot \cos(\theta_i) \tag{6}$$

$$F_{Y_i} = \sum_{i=1}^{N} F_{\zeta\,i} \cdot \sin(\theta_i) \tag{7}$$

Figure 34 shows the predicted static load as a function of the shaft deflection, as well as the experimental results obtained at position 1-5 for CFB1, see Figure 7. The predicted loads are determined from the parameters noted in Figure 34. Note that a third order polynomial fits well the predicted load. Notice also in the predictions the flat section at small deflections, which represents the gap between the shaft and the bearing due to the nominal clearance. On the other hand, the flat region from the experimental load versus deflection curve is less evident than with in the analytical results. The predictions in Figure 34 are obtained for a dry friction coefficient μ_f = 0.1 and for a bump half length, l_o = 0.08 in.

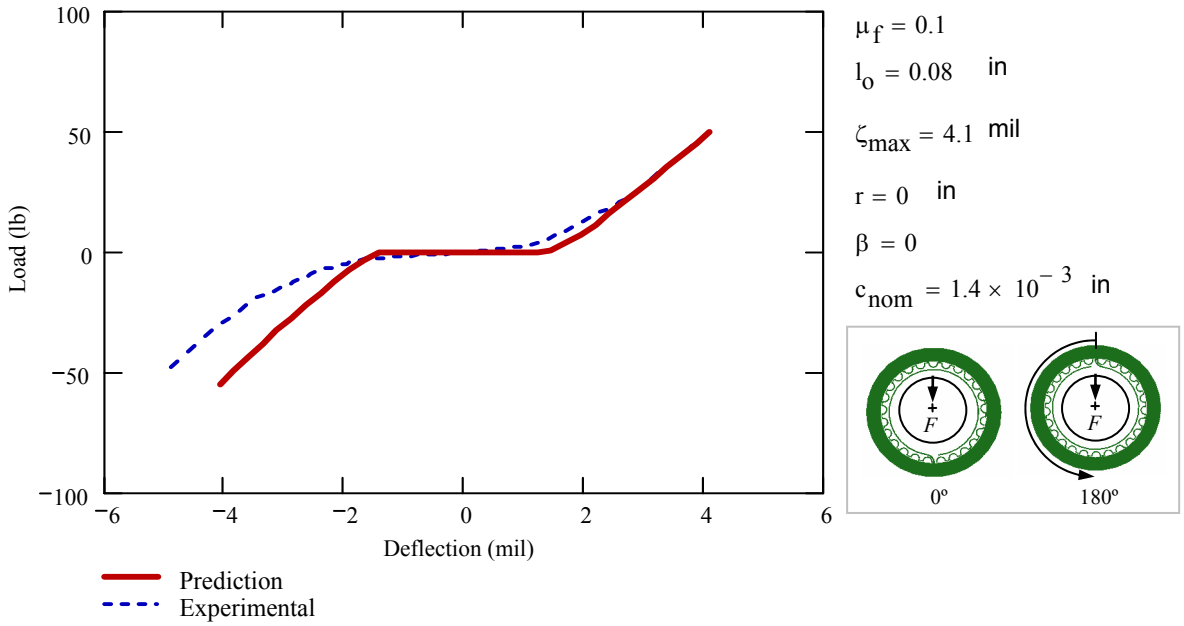

Figure 34 Predicted and Experimental Load versus Bearing Deflection Curves for Position 1-5 (0º-180º). (Shaft Diameter D_1 = 1.500 in; μ_f = 0.1; l_o = 0.08 in)

Figures 35 and 36 show the predicted and experimental load versus deflection curves for two different values of l_o; i.e. 0.085 in and 0.07 in, respectively. These analytical results are obtained for a constant values of μ_f = 0.1. Predicted forces in Figures 35 and 36 are obtained for the same input data as the predicted forces in Figure 33. The experimental curve displays the results for positions 1-5, see Figure 7.a.

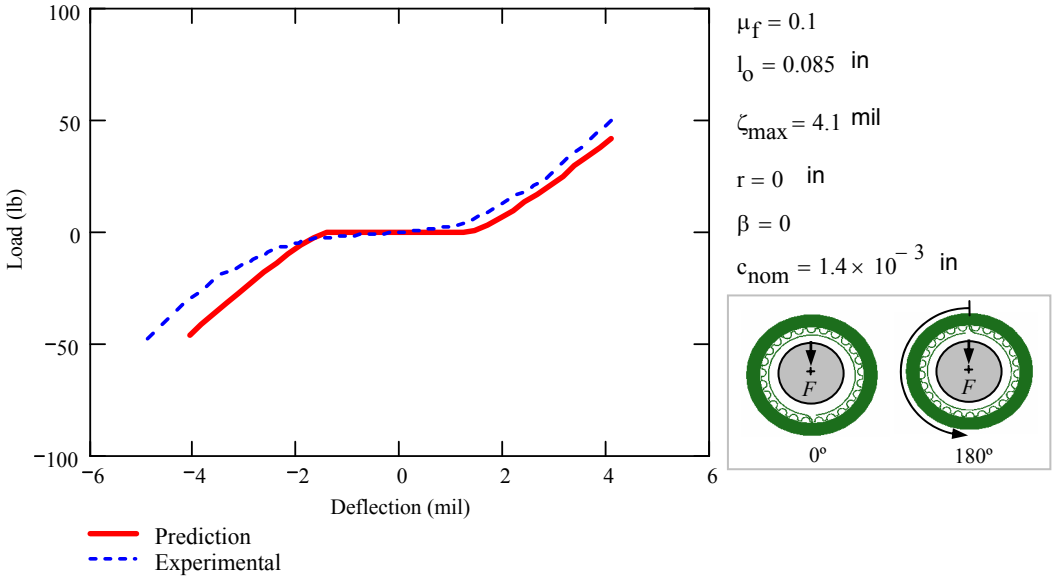

Figure 35 Predicted and Experimental Load versus Bearing Deflection Curves for Position 1-5 (0º-180º). (Shaft Diameter D_1 = 1.500 in; μ_f = 0.1; l_o = 0.085 in)

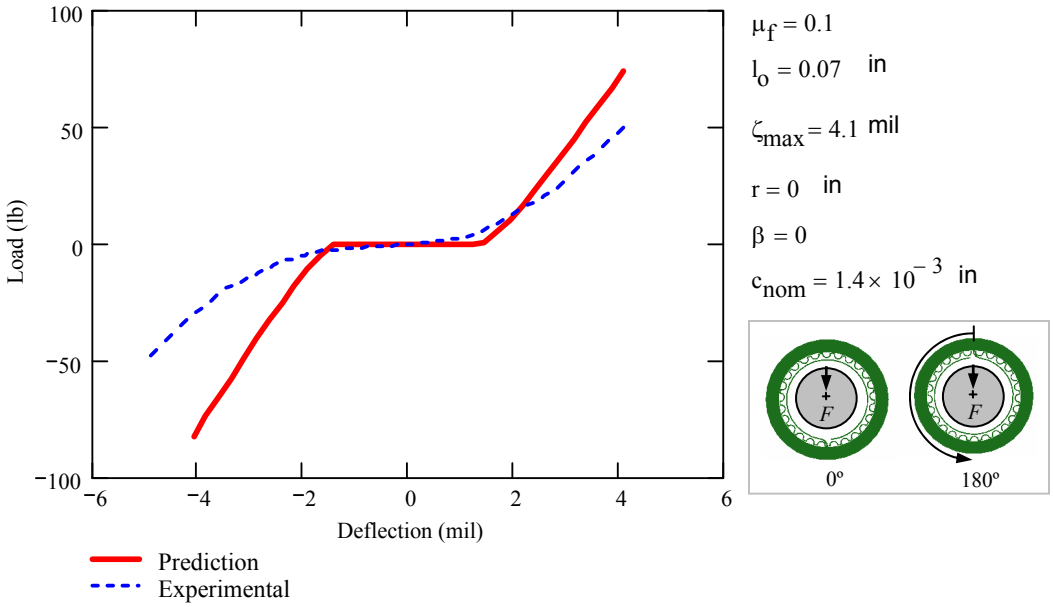

Figure 36 Predicted and Experimental Load versus Bearing Deflection Curves for Position 1-5(0º-180º). (Shaft Diameter D_1 = 1.500 in; μ_f = 0.1; l_o = 0.07 in)

Analytical prediction of the foil bearing load versus deflection are obtained for different bump length values, as shown in Figures 34 through 36. The agreement of the experimental and the analytical results is determined by comparing the shaft displacements of both curves (predicted and experimental) at the maximum static load reached in the static tests, i.e. 50 lb. Table 10 shows the theoretical shaft displacement for different bump lengths at the maximum static load reached in the static experiments, i.e. 50 lb. Note that the bump length can not exceed the value of the bump pitch. Therefore, l_o can not be larger than 0.09 in.

Table 10 Prediction of Rotor Displacements at ± 50 lb over Different Values of Bump Length. Experimental Values of Bearing Deflection = 5 mil. (Position 1- 5 (0º - 180º); μ_f = 0.1; r = 0; Nominal Foil Bearing Dimensions)

l_o [in]	Rotor Displacement [mil] Predictions	Error Percent Difference (%)
0.06	2.65	47
0.07	3.13	37.4
0.08 (Nominal)	3.85	23
0.085	4.1	18

Table 10 indicates that increasing the bump length ($2_x l_o$) the predicted rotor deflection approaches the experimental value of bearing deflection at 50 lb, i.e. 5 mil, i.e. for l_o = 0.085 in. the percentage deviation with respected to the experimental result is 18% while for l_o = 0.06 in. the percent difference is 47 %. Note also that the larger bump length values the smaller the structural stiffness, i.e. after the flat region, the slope (stiffness) of the force versus deflection curve for l_o = 0.085 in. (see Figure 35) is lower than the slope (stiffness) of the curve for l_o = 0.07 in. (see Figure 36).

As mentioned before, the foil bearing structural stiffness is also sensitive to the dry friction coefficient. Figure 37 shows the influence of the friction coefficient on the foil bearing structural stiffness. Increasing the value of the friction coefficient renders larger reaction forces. A friction coefficient from 0.01 to 0.2 renders the best agreement with the experimental results, implying that low friction coefficients are governing the structural characteristics in the test foil bearings.

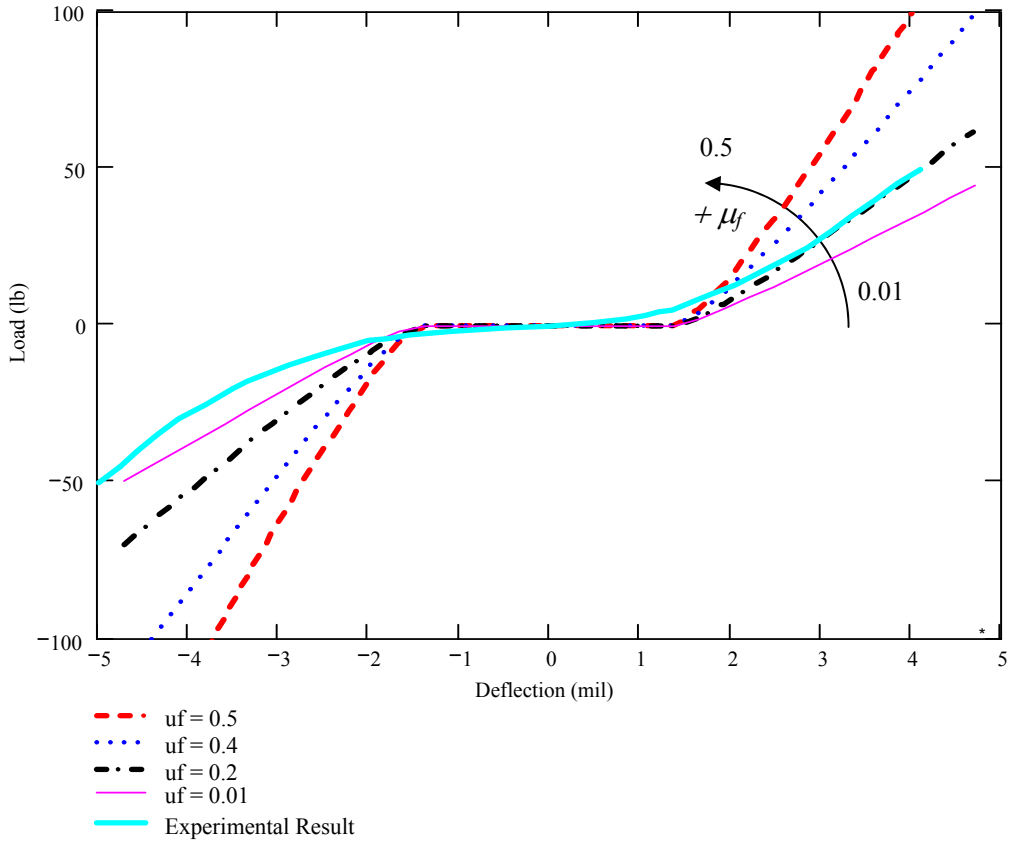

Figure 37 Predicted Load versus Bearing Deflection Curves for Increasing Dry Friction Coefficients. (Positions 1- 5 (0°-180°); Shaft Diameter D_1; l_o = 0.08 in)

Table 11 shows the effect of radial clearance variations on the force versus deflection prediction curves. Recall that the nominal radial clearance for a 1.500 in shaft diameter is 0.0014 in. The maximum deviation of the predicted force versus deflection curve from the experiment data is determined at ± 50lb. Note that for radial clearances from 0.0013 in. to 0.0015 in., the

maximum rotor displacement deviation is observed at -50 lb, as shown in Table 11. Conversely, radial clearances of 0.0016 in. and 0.0017 in. yields on maximum rotor displacement at 50 lb. Table 11 shows that changes on the radial clearance does not significantly affect the correlation between the predictions and the experimental results, i.e. the maximum error percent difference is 18% when the nominal clearance increases approximately by 20 %.

Table 11 Prediction of Rotor Displacements at ± 50 lb for Different Values of Radial Clearance. (Position 1 – 5 (0º-180º); μ_f = 0.1; r = 0; Nominal CFB1 Dimensions)

c_{nom} [in]	Rotor Displacement [mil]		Error Percent Difference [%]
	Predictions	Experimental Value	
0.0013	4.18	5.00 at - 50 lb	16.6
0.0014 (Nominal)	4.29	5.00 at - 50 lb	14.8
0.0015	4.42	5.00 at - 50 lb	11.6
0.0016	4.54	4.1 at 50 lb	15.4
0.0017	5.00	4.1 at 50 lb	18

Force versus deflection predictions are obtained over different foil bearing parameters, providing relevant information about uncertain parameters in the experimental results, such as the dry friction coefficient and the radial clearance. Figures 34 through 37 show the predicted loads and deflections for a wide range of friction coefficients and bump lengths. Analytical results correlate best with experimental results when friction coefficients are low, i.e. μ_f ranging from 0.01 to 0.2; and when the bump length is selected within a range of 0.085 ± 5%. Note that the effect of the friction coefficient on a single bump structural stiffness (see Figure 30) is not significant at low values of μ_f, i.e. 0.01 to 0.2. Therefore, changes of the friction coefficient within this range do not affect significantly the foil bearing structural stiffness.

Predicted foil bearing structural stiffnesses are derived from the force versus deflection relationship. The dry friction coefficient and the bump length are selected as, μ_f =0.1 and l_o = 0.085 in., respectively. Predictions of structural stiffness are conducted for different angular positions and bearing preloads and are calculated by taking the first derivate of the force versus deflection curve fit. Figure 38 shows the predicted structural stiffness with no bearing preload (r = 0), and also shows the identified structural stiffness from the experimental results for a D_1 nominal shaft diameter. Figures 38 and 40 show the predicted and experimental foil bearing structural stiffness for the two other shaft diameters, D_2 = 1.501 in. and D_3 = 1.499 in., respectively. The structural stiffness experimental values in Figures 37 through 39 are taken for positions 1–5 (0º-180º), see Figure 7.a.

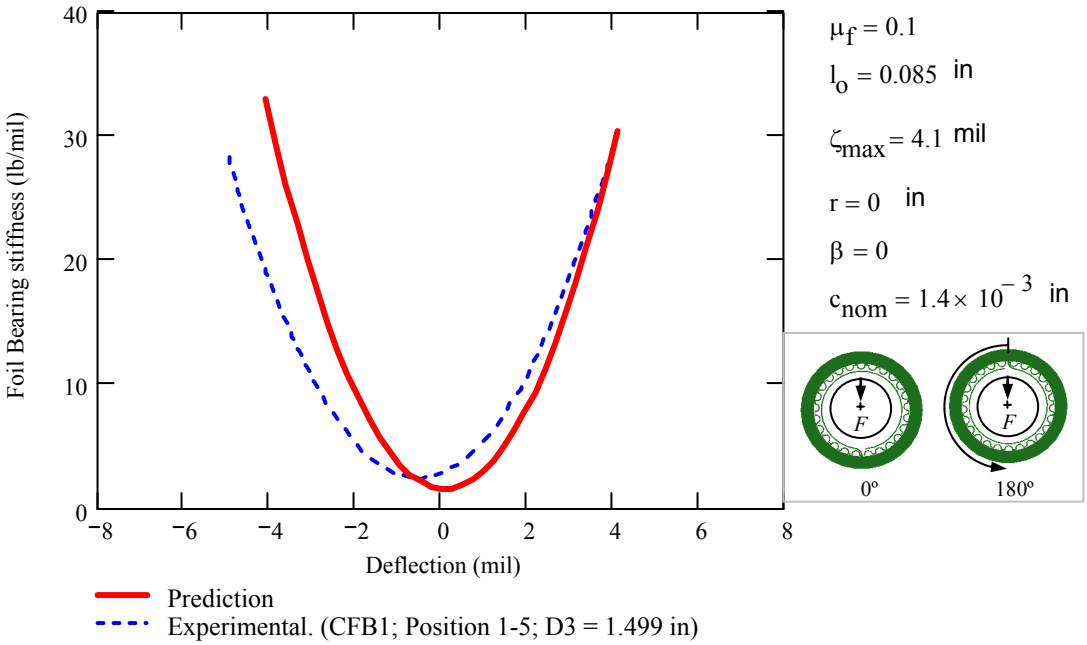

Figure 38 Predicted and Experimental Structural Stiffness versus the Shaft Deflection (Shaft Diameter D_1 =1.500in; μ_f = 0.1; l_o = 0.085 in; r = 0 in)

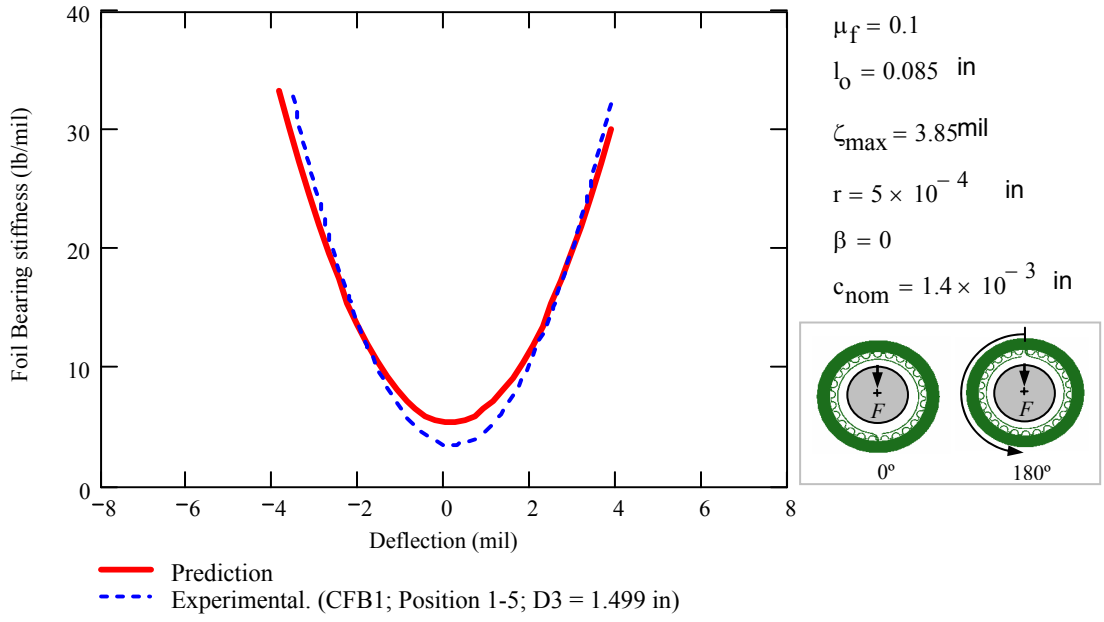

Figure 39 Predicted and Experimental Structural Stiffness versus the Shaft Deflection (Shaft Diameter D_2 =1.501 in; μ_f = 0.1; l_o = 0.085 in; r = 0.5 mil)

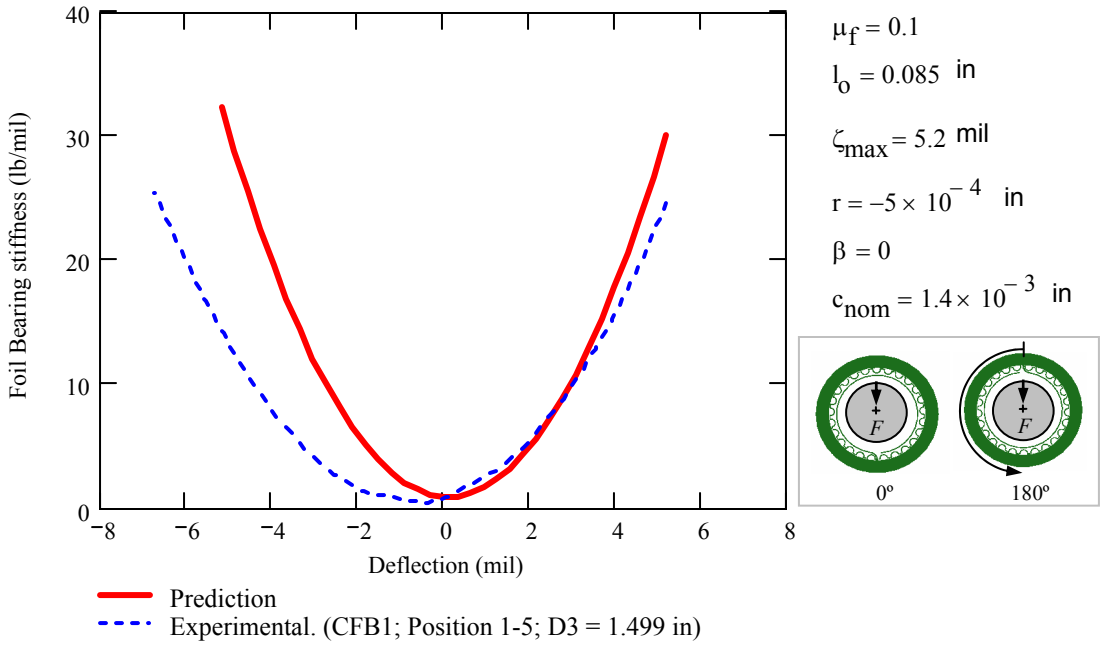

Figure 40 Predicted and Experimental Structural Stiffness versus the Shaft Deflection (Shaft Diameter D_3 =1.499 in; μ_f = 0.1; l_o = 0.085 in; r = - 0.5 mil)

Figures 38 through 40 show similar structural stiffness for the predicted and experimental results. Predicted structural stiffness correlates best with the experimental results when the bearing is preloaded. Slightly differences are noted when the shaft diameter is D_3 = 1.499 in. Table 12 presents a correlation between the theoretical predictions and the measurements of the foil bearing maximum structural stiffness. Table 12 also shows the error percent difference between the theoretical predictions and the experimental data. In general, the maximum predicted structural stiffness correlates accurately with the experimental results. However, some inconsistencies are observed at positions 1 – 5 for a shaft diameter of 1.499 in, where the error percentage reaches the maximum vale of 21%. The rest of the percentages are within a 15% of error.

Figure 41 shows the behavior of the foil bearing structural stiffness with respect to the static load. Analytical results of structural stiffness present a good agreement when approximating the structural stiffness from the load versus deflection curve fit. Figure 41 shows the experimental results of structural stiffness for positions 3 – 7 (90°-270°), therefore the structural stiffness is predicted at β = 90°.

Table 12 Experimental and Theoretical Correlation of Maximum Foil Bearing Structural Stiffness (μ_f = 0.1; l_o = 0.085 in; c_{nom} = 0.0028 in)

Shaft Diameter	Angular Position	Predictions	Experimental Data	Error Percent Difference
		Maximum Stiffness [lb/mil]		
D_1 (r = 0)	1 – 5 (0° - 180°)	33.57	30.45	10.25
	2 – 6 (45° - 225°)	30.97	32.65	5.14
	3 – 7 (90° - 270°)	33.04	32.25	2.69
	4 - 8 (135° - 315°)	33.29	33.84	1.63
D_2 (r = 0.5 mil)	1 – 5	34.10	34.61	1.47
	2 – 6	33.51	39.45	15.06
	3 – 7	33.49	39.27	14.72
	4 – 8	33.43	35.52	5.88
D_3 (r =- 0.5 mil)	1 – 5	33.28	26.06	21.69
	2 – 6	29.85	29.10	2.58
	3 – 7	32.29	32.51	0.68
	4 – 8	33.47	30.57	8.66

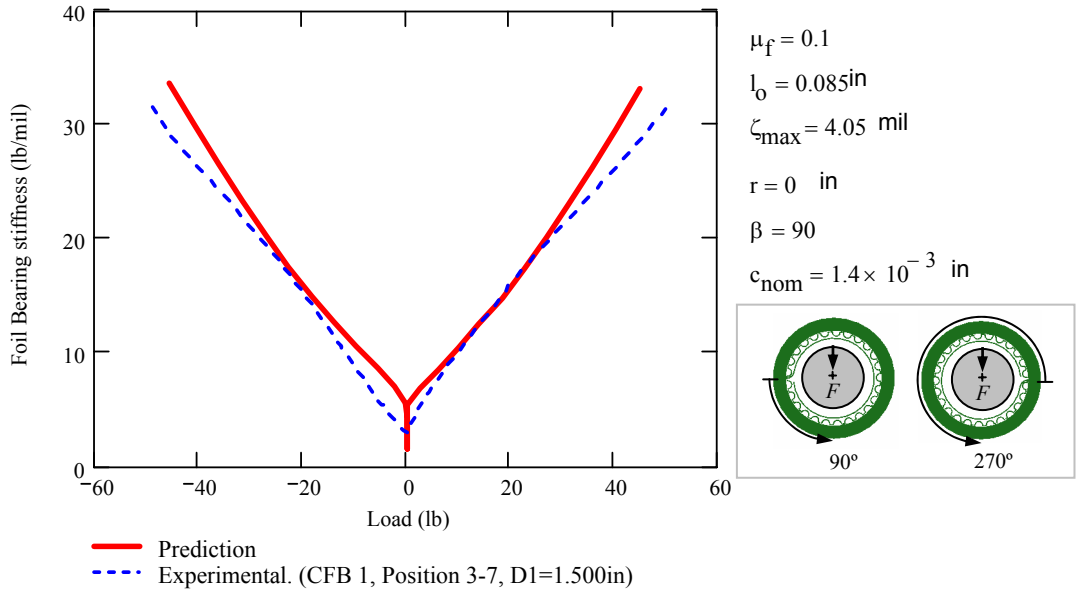

Figure 41 Predicted and Experimental Structural Stiffness with respect to the Static Load. (Shaft Diameter D_3 =1.500 in; μ_f = 0.1; l_o = 0.085 in; r = 0)

Figure 42 presents the effect of large bearing preloads on the structural stiffness predictions. Three different preloads larger than the nominal clearance are selected to evaluate their influence on the structural stiffness, as noted also in Figure 42. The predicted structural stiffness behaves in an opposite manner as the previous results when using small bearing preloads. This peculiar behavior arises because the journal is entirely wrapped by all the twenty five bumps (springs). Therefore, at small loads and deflections every bump contributes to the foil bearing structural stiffness. Indeed, when loading the foil bearing at one specific angular position the bumps located at the opposite direction of the applied load generate a force in the same direction as the loading force on the foil bearing, thus producing a higher foil bearing structural stiffness. When the applied load to the foil bearing increases the forces at the opposite direction of the applied load become smaller because the bumps (springs) are less compressed. Finally, when there is no contact between the journal and the bumps at the opposite direction of the applied load, the foil bearing structural stiffness is determined by the stiffness of the bump located near to the location of the load.

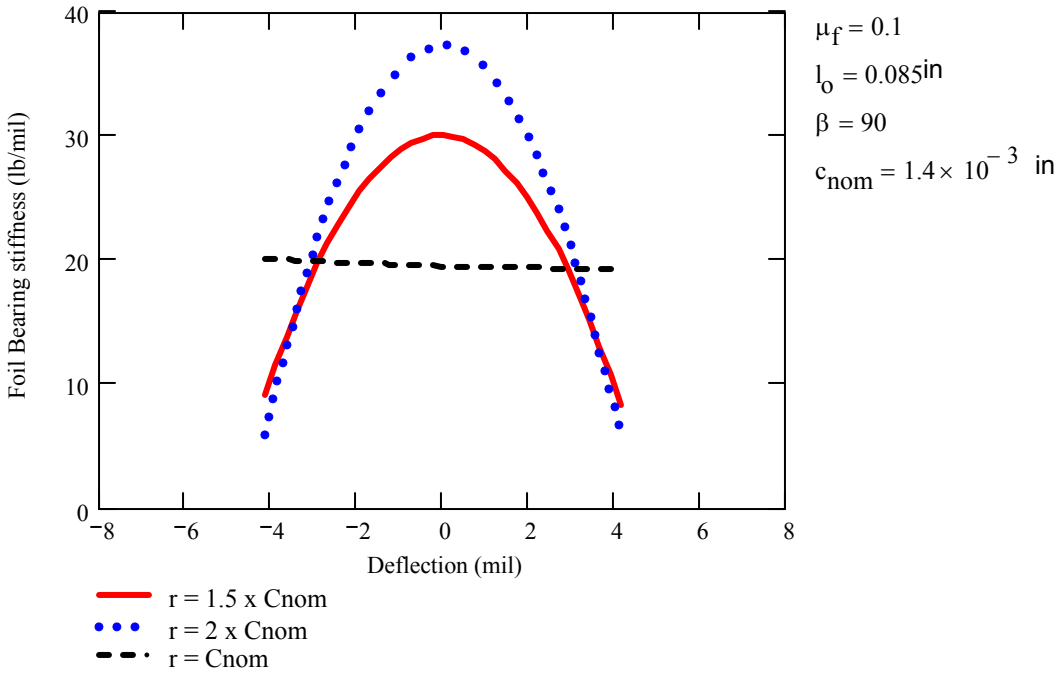

Figure 42 Predicted Structural Stiffness for Different Bearing Preloads Larger than the Nominal Clearance. (Shaft Diameter D_1 = 1.500 in; μ_f = 0.1; l_o = 0.085 in)

The model advanced provides reliable results of foil bearing structural stiffness for a selected range of foil bearing parameters. The effect of the friction coefficient plays an important role on the structural stiffness behavior of the foil bearing, i.e. high friction coefficients produce larger structural stiffness. The bump length is also an important parameter when studying the foil bearing structural stiffness behavior. The structural stiffness increases significantly when the bump length decreases even to a small fraction of its nominal dimension.

VII. CONCLUSIONS

Gas foil bearings satisfy most of the requirements noted for oil-free turbomachinery applications. However, there is a noticeable absence of experimental verification for the rotordynamic performance of gas foil bearings, including the bearing underlying elastic structural properties. The open literature provides little insight except for infamous commercial claims.

Four bump-type foil bearings (CFBs) were acquired in 2002 from Foster-Miller Technologies. The bearings, with length equal to 1.50 in, consist of a Teflon coated foil (0.004 in thickness) supported on 25 bumps, whose height and pitch equal 0.015 in and 0.18 in, respectively. The CFBs were designed to operate with a shaft of nominal diameter equal to 1.50 in. The manufacturer provided a radial clearance of 1.4 mils for the nominal configuration. A simple test set up was assembled to measure the CFB deflections resulting from increasing static loads applied radially at various angular positions around the bearing. The experiments were conducted with three shafts, one with the nominal diameter of 1.50 in; and the other shafts with diameters +1 mil and –1 mil larger (smaller) than the nominal one. The different shafts induce a degree of preload into the CFB.

The static measurements show different deflection versus load characteristics depending on the orientation of the applied static load relative to the position of the foil spot weld. The experimental results also demonstrate that the applied load is nonlinear relative to the structure deflection, a third degree polynomial describing well the recorded behavior. Static loading and unloading tests evidence a characteristic hysteresis due to the dry friction between the bumps and the bearing housing. The CFB structural stiffness derived from the load versus deflection tests increases nonlinearly as the radial deflection increases (hardening effect). The estimated structural stiffness coefficients obtained from two bearings, identical in construction, also differ. The radial preload results in important changes in the CFB stiffness, in particular for small load conditions.

Predictions show that the stiffness of a single bump is most sensitive to the dry-friction coefficient, the bump length, and the bump-ends conditions, i.e. welded or free to move. A simple physical model assembles the individual bump stiffnesses and renders predictions for the CFB radial stiffness as a function of the bump geometry and material parameters, dry-friction coefficient, load orientation, radial clearance and initial preload. The model predicts well the physical behavior, including the apparent nonlinearity, i.e. hardening effect at large loads. In general, predicted structural stiffnesses correlate well with the experimentally derived coefficients for the largest load condition.

The large uncertainty in the actual clearance (if any) upon assembly of the shaft into a CFB affects most the predictions. The (yet unknown) dry-friction coefficients, between the bumps and foil, and between bumps and bearing housing, are also important. Dynamic force experiments are currently being performed to assess the actual dissipation characteristics in the test foil bearings.

VIII. REFERENCES

[1] Agrawal, G. L., 1997, "Foil Air/Gas Bearing Technology—An Overview," International Gas Turbine & Aeroengine Congress & Exhibition, Orlando, Florida, ASME paper 97-GT-347.

[2] Ku, C.-P, and, H., Heshmant, 1992, "Complaint Foil Bearing Structural Stiffness Analysis Part I: Theoretical Model - Including Strip and Variable Bump Foil Geometry," ASME Journal of Tribology, Vol. 114, No. 2, pp. 394-400.

[3] Agrawal, G. L., 1998, "Foil Air Bearings Cleared to Land," Mechanical Engineering, pp. 78-80, July.

[4] Ku, R., and, H., Heshmant, 1992, "Compliant Foil Bearing Structural Stiffness Analysis," ASME Journal of Tribology, Vol. 113, No.1, pp.364-369.

[5] Iordanoff, I., 1999, "Analysis of an Aerodynamic Complaint Foil Thrust Bearing: Method for a Rapid Design," ASME Journal of Tribology, Vol. 121, pp.816-822.

[6] DellaCorte, C., and, M., Valco, 2000, "Load Capacity Estimation of Foil Air Journal Bearing for Oil-Free Turbomachinery Applications," Tribology Transactions, Vol. 43, No. 4, pp. 795 – 801.

[7] Chen, H., R., Howarth, B., Geren, J., Theilacker, and, W., Soyars, 2001, "Application of Foil Bearing to Helium Turbocompresor," Proceedings of the 30th Turbomachinery Symposium, pp. 103-112, Houston, TX.

[8] Howard, S., and, C., Della Corte, 2001, "Dynamic Stiffness and Damping Characteristics of a High-Temperature Air Foil Journal Bearing," Tribology Transactions, Vol. 44, No. 4, pp. 657 – 663.

[9] Ku, C.-P, and, H., Heshmant, 1993, "Complaint Foil Bearing Structural Stiffness Analysis Part II: Experimental Investigation," ASME Journal of Tribology, Vol. 113, No.3, pp. 364-369.

[10] Heshmat, H., 1994, "Advancements in the Performance of Aerodynamic Foil Journal Bearings: High Speed and Load Capability," ASME Journal of Tribology, Vol. 116, pp 287 – 295.

[11] Lu, Y.P., and, C.T., Sun, 1995, *Vibration Damping of Structural Elements*, Prentice Hall PTR, pp. 6 -7.

[13] Coleman, H., and, W., Steele, 1985, *Experimentation and Uncertainty Analysis for Engineers*, Wiley-Interscience Publications, pp. 33-35.

APPENDIX A. FOIL BEARING NOMINAL DIMENSIONS (SI UNITS)

Table A 1 Foil Bearing Nominal Dimensions (SI)

Parameters	CFB 1	CFB 2	CFB Manufacturer Data
Outer Diameter (cm)	5.104	5.102	-----
Foil Thickness (mm)	0.157	0.157	0.102
Number of Bumps	25	25	25
Pitch (mm) (deg)	4.635 (13)	4.628 (13)	4.572
Bump Length (cm)	0.4064	0.4064	N/A
Axial Length (cm)	3.834	3.823	----
Bump Foil Thickness (mm.)	N/A	N/A	0.1016
Bump height (mm.)	N/A	N/A	0.381
Poisson's Ratio	N/A	N/A	0.29
Modulus of Elasticity (Pa)	N/A	N/A	213736.4
Inner Diameter Ave. (cm.)	3.835	3.831	3.817
Nominal Clearance [mm] [11]	N/A	N/A	0.0355

[11] Nominal Clearance for a shaft diameter of 1.500 in

APPENDIX B. DIFFERENCES BETWEEN MEASUREMENTS CONDUCTED WITH AN EDDY CURRENT SENSOR AND A DIAL GAUGE. CFB1

In conducting the static experiments with a dial gauge and with an eddy current sensor the following features affected the measurements:

- The uncertainty of the dial gauge, U_X is larger than the uncertainty of the eddy current sensor, U_S, i.e. $U_X = 0.5$ mil and $U_S = 0.05$ mil, respectively.
- Different shafts were used in measurements. Tests using a dial gauge were performed with a copper shaft of 1.500 in. in diameter, while tests using an eddy current sensor used a stepped shaft for three different shaft diameters.
- Dial gauge is more sensitive to misalignment than eddy current sensors.
- Experiment with eddy current sensor and dial gauge were performed on different dates. Therefore, the test setup was disassembled and assembled to conduct the new experiments

Measurements of foil bearing deflection with an eddy current sensor and a dial gauge are shown in Figure B1. The identified structural stiffnesses with the two instruments are shown in Figure B2. The results show in Figures B1 and B2 are obtained from positions 1 – 5, see Figure 7a.

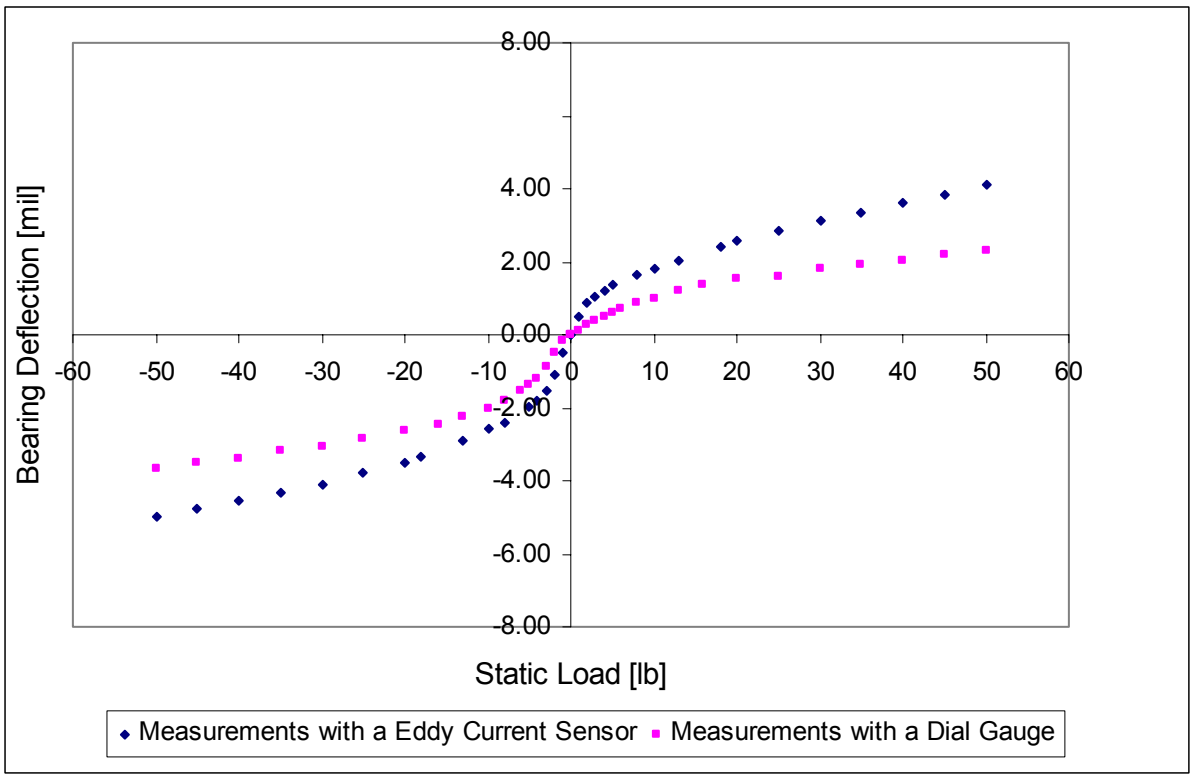

Figure B 1 Bearing Deflection Measurements with a Eddy Current Sensor and with a Dial Gauge

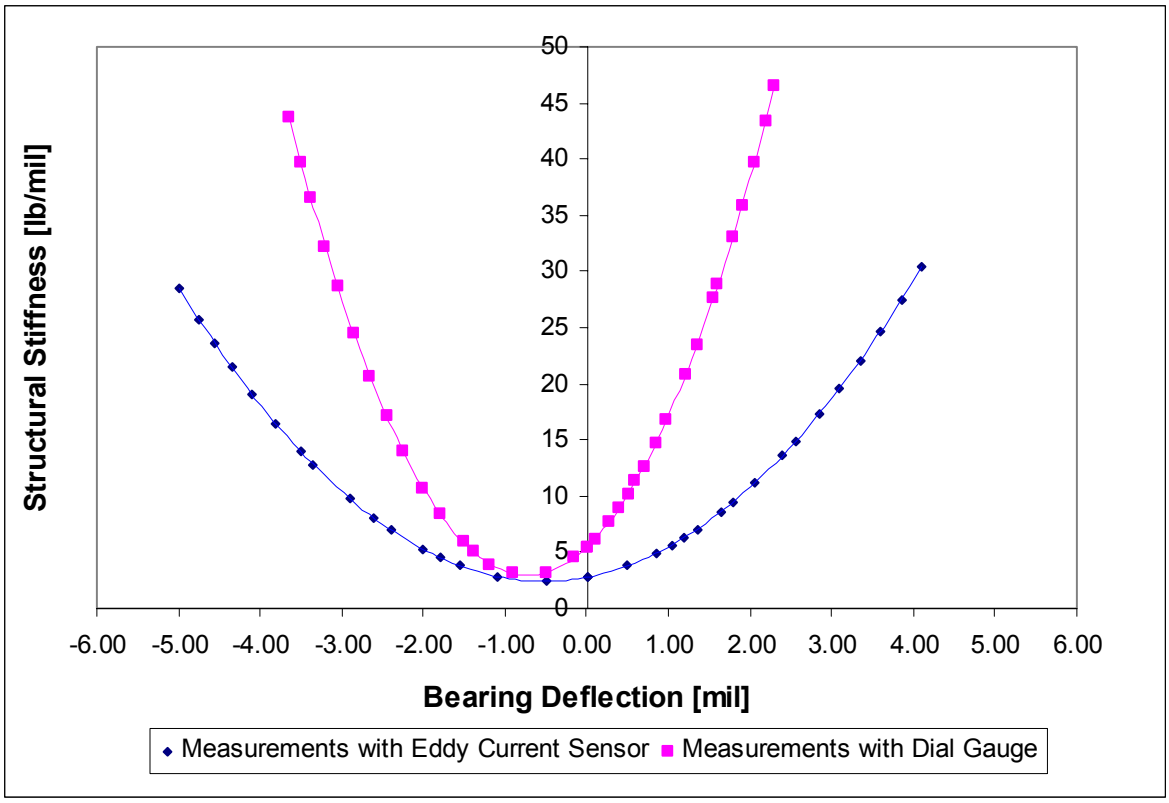

Figure B 2 Identified Bearing Structural Stiffness for two Different Displacement Sensors (Eddy Current Sensor and Dial Gauge)

APPENDIX C. UNCERTAINTY ANALYSIS

The bearing stiffnesses derived have an uncertainty associated with the data reduction applied to obtain these values. Since the bearing stiffness cannot be measured directly with an instrument, it is not possible to assign a unique value of uncertainty or associate it with the instruments used. Therefore, a general uncertainty analysis must be applied to assess the accuracy of the stiffnesses obtained. According to Coleman [11], the uncertainty analysis consists of determining how the uncertainties in the individual variables propagate though a data reduction equation into a result. This analysis is applied into the bearing stiffness calculations and the procedure is explained below.

The relationship between the static load and the bearing deflection has a third order polynomial tendency. Values of bearing stiffness are calculated from equations (see Tables 4 and 5), and the behavior of the identified bearing stiffnesses with respect to the static load and bearing deflection are shown on Figures 13, 14 16 and 17. These graphs show a second order polynomial dependency of the bearing stiffness with respect to the deflection, and a linear dependency of the bearing stiffness with respect to the applied load. A general analysis of the bearing stiffness uncertainty follows in order to show the procedure applied to obtain the values of uncertainty associated with bearing stiffness.

The general analysis consists on studying the expression of stiffness (k) derived from the third polynomial curve fit of the load and deflection measurements. This expression is

$$k = a\,x^2 + b\,x + c \tag{8}$$

where a, b and c are constants obtained from the curve fits to the test data.

The bearing stiffness (k) is a parameter estimated from the experimental results, and depends on two variables, load (F) and deflection (x), i.e.

$$k = f(x, F) \tag{9}$$

According to Coleman, the uncertainty (U_r) of an experimental result (r), a function of J variables X_i, is given by:

$$U_r = \left\{ \left[\left(\frac{\partial r}{\partial X_1} \right) \cdot U_{X_1} \right]^2 + \left[\left(\frac{\partial r}{\partial X_2} \right) \cdot U_{X_2} \right]^2 + \ldots + \left[\left(\frac{\partial r}{\partial X_j} \right) \cdot U_{X_i} \right]^2 \right\}^{1/2} \tag{10}$$

Applying Equation (10) to the structural stiffness uncertainty renders Equation (9) and (10), depending on the displacement instrument used (dial gauge and eddy current sensor)

$$U_k = \left\{ \left[\left(\frac{\partial k}{\partial F} \right) \cdot U_F \right]^2 + \left[\left(\frac{\partial k}{\partial x} \right) \cdot U_X \right]^2 \right\}^{1/2} \tag{11}$$

and,

$$U_k = \left\{ \left[\left(\frac{\partial k}{\partial F} \right) \cdot U_F \right]^2 + \left[\left(\frac{\partial k}{\partial V} \right) \cdot U_V \right]^2 \right\}^{1/2} \tag{12}$$

where U_F is the uncertainty of the dynamometer. (±0.5lb), U_X is the uncertainty of the dial gauge (±0.05mil) and U_V is the uncertainty the multimeter (±0.01V). Eddy current sensors gain G = 0.200 V/mil.

Equation (11) and (12) involve three derivates of the structural stiffness versus the static load (F), the bearing deflection (x) and the voltage output (V). These derivates are given by the following expressions

$$\frac{\partial k}{\partial x} = \frac{\partial f}{dx} \tag{13}$$

$$\frac{\partial k}{\partial F} = \frac{\partial f}{\partial F} = \frac{\partial f}{\partial x} \cdot \frac{\partial x}{\partial F} \tag{14}$$

and,

$$\frac{\partial k}{\partial V} = \frac{\partial f}{\partial V} = \frac{\partial f}{\partial x} \cdot \frac{\partial x}{\partial V} \tag{15}$$

Note that the term $\partial x / \partial V$ on Equation (15) represents the inverse of the eddy current sensor gain; $1/G$.

Substituting equations (13) and (14) in equation (11), and equations (14) and (15) in equation (12) the resulting expressions of structural stiffness uncertainty are

$$U_k{}^2 = \left(\frac{\partial f}{\partial x} \right)^2 \cdot U_x{}^2 + \left(\frac{\partial f}{\partial x} \cdot \frac{\partial f}{\partial F} \right)^2 \cdot U_F{}^2 \tag{16}$$

and,

$$U_k{}^2 = \left(\frac{\partial f}{\partial x} \cdot \frac{\partial x}{\partial V} \right)^2 \cdot U_V{}^2 + \left(\frac{\partial f}{\partial x} \cdot \frac{\partial x}{\partial F} \right)^2 \cdot U_F{}^2 \tag{17}$$

The simplified expression of equations (11) and (12) are

$$U_k = \left| \left(\frac{\partial f}{\partial x} \right) \cdot U_x \right| \left[1 + \left(\frac{\partial x}{\partial F} \right)^2 \cdot \frac{U_F{}^2}{U_x{}^2} \right]^{1/2} \tag{18}$$

and,

$$U_k = \left| \left(\frac{\partial f}{\partial x} \right) \right| \left[\left(\frac{\partial x}{\partial F} \right)^2 \cdot (U_F)^2 + \left(\frac{\partial x}{\partial V} \right)^2 \cdot (U_V)^2 \right]^{1/2} \tag{19}$$

where the derivate of the deflection with respect to the static load ($\partial x / \partial F$) can be obtained using the following basic relationship

$$\frac{\partial x}{\partial F} = \frac{1}{\frac{\partial F}{\partial x}} \tag{20}$$

Equation (18) represents the structural stiffness uncertainty when using a dial gauge, while equation (19) represents the structural stiffness uncertainty when using an eddy current sensor.

Equations (18) and (19) depend on the bearing deflection and the uncertainties of the dynamometer and displacement instrument. Evaluating Equations (18) and (19) over the whole span of measurements of bearing deflections and loads, the structural stiffness uncertainty is obtained for all angular positions and shaft diameters.

The bearings stiffness uncertainty is calculated at every angular position. Table 6 shows values of stiffness uncertainty for measurements at positions 1 - 5 for CFB1. Results show that the bearing stiffness percentage uncertainty decreases as the static load increases, i.e. for bearing 1 at position 1 the bearing stiffness at 1 lb is 7.59 lb/mil and the percentage uncertainty is 7.8%; while at 50 lb the percentage uncertainty is 3% for a bearing stiffness of 44.66 lb/mil.

Averages of bearing structural stiffness are obtained at two static loads for different shaft diameter, as shown in Table 6. The goodness of this average with respect of the collection of pairs (structural stiffness, angular position) is obtained by using the standard error of an estimate (*SEE*). The *SEE*, represents the deviation of the average structural stiffness from the data set.

$$SEE = \left[\frac{\sum_{i=1}^{N} [K_i - K_A]^2}{N - 2} \right]^{1/2} \tag{21}$$

where N is the number of data set points. K_A is the average structural stiffness and K_i represent the value of structural stiffness at each data set point.

APPENDIX D. **FORMULAE FOR PREDICTION OF SINGLE BUMP STIFFNESS**

Bump foil structural stiffness
Based on Iordanoff formulae [5]

$h := 0.015\ in$ Reference bump height

$s := 0.18\ in$ Pitch (distance)

$l_o := 0.07\ in$ Reference 1/2 length

$t := 0.004\ in$ Foil thickness

$Axial := 1.5\ in$ Axial lengh of the foil bearing

$Strips := 5$ Number of bumps strips

$L := \frac{Axial}{Strips}$ Lenght of one bump

$E := 31000000\ psi$ Young modulus

$\nu := 0.29$ Poisson ratio

$\mu_f := 0.1$ $\frac{h}{l_o} = 0.214$

$p := s$

STIFFNESS for free-bump

$$Kf(\mu_f, l_o, h, s, t) := \left| \begin{array}{l} R \leftarrow \frac{\left(l_o^2 + h^2\right)}{2 \cdot h} \\ \alpha \leftarrow 2 \cdot \operatorname{acos}\left(\frac{l_o}{R}\right) \\ A \leftarrow \sin\left(\frac{\alpha}{2}\right) + \mu_f \cdot \cos\left(\frac{\alpha}{2}\right) \\ I \leftarrow \left(A^2 + \frac{1 + \mu_f^2}{2}\right) \cdot \frac{\alpha}{2} - \frac{\left(1 - \mu_f^2\right)}{4} \cdot \sin(\alpha) - \frac{\mu_f}{2} \cdot (\cos(\alpha) - 1) - 2 \cdot A \cdot \left(1 - \cos\left(\frac{\alpha}{2}\right) + \mu_f \cdot \sin\left(\frac{\alpha}{2}\right)\right) \\ compliance \leftarrow \frac{\left[6 \cdot l_o^3 \cdot s \cdot I \cdot \left(1 - \nu^2\right)\right]}{E \cdot t^3 \cdot \left(\sin\left(\frac{\alpha}{2}\right)\right)^3} \\ \text{return } \frac{L \cdot s}{compliance \cdot 1000} \end{array} \right.$$

STIFFNESS for welded-(pinned) bump

$$
\begin{aligned}
Kp(\mu_f, l_o, h, s, t) := \;& R \leftarrow \frac{\left(l_o^{\,2} + h^2\right)}{2\cdot h} \\
& \alpha \leftarrow 2\cdot \operatorname{acos}\left(\frac{l_o}{R}\right) \\
& y_a \leftarrow \frac{-\left(\frac{3}{4}\cdot\sin(\alpha) - \frac{\alpha}{4} - \sin\left(\frac{\alpha}{2}\right)\right)}{\alpha\cdot\sin\left(\frac{\alpha}{2}\right)\cdot\left(\sin\left(\frac{\alpha}{2}\right) + \mu_f\cdot\cos\left(\frac{\alpha}{2}\right)\right) - 2\cdot\mu_f\cdot\left(\sin\left(\frac{\alpha}{2}\right)\right)^2 + \frac{\alpha}{2} - \frac{\sin(\alpha)}{2}} \\
& J \leftarrow y_a\cdot\left[\left(\cos\left(\frac{\alpha}{2}\right) - 1\right)\cdot\left(\sin\left(\frac{\alpha}{2}\right) + \mu_f\cdot\cos\left(\frac{\alpha}{2}\right)\right) + \mu_f\cdot\frac{(1-\cos(\alpha))}{4}\right] + (1 - y_a)\cdot\left(\frac{\alpha}{4} - \frac{\sin(\alpha)}{4}\right) \\
& \text{compliance} \leftarrow \frac{\left[12\cdot l_o^{\,3}\cdot s\cdot J\cdot\left(1-\nu^2\right)\right]}{E\cdot t^3\cdot\left(\sin\left(\frac{\alpha}{2}\right)\right)^3} \\
& \text{return } \frac{L\cdot s}{\text{compliance}\cdot 1000}
\end{aligned}
$$